

UNIVERSITY OF OKLAHOMA

GRADUATE COLLEGE

A TALE OF TWO MESOVORTICES: ANALYSIS OF A SIMULATED SEVERE  
MCS OBSERVED BY PECAN ON 5-6 JULY 2015

A THESIS

SUBMITTED TO THE GRADUATE FACULTY

in partial fulfillment of the requirements for the

Degree of

MASTER OF SCIENCE IN METEOROLOGY

By

MATTHEW DOUGLAS FLOURNOY

Norman, Oklahoma

2017

A TALE OF TWO MESOVORTICES: ANALYSIS OF A SIMULATED SEVERE  
MCS OBSERVED BY PECAN ON 5-6 JULY 2015

A THESIS APPROVED FOR THE  
SCHOOL OF METEOROLOGY

BY

---

Dr. Michael Coniglio, Chair

---

Dr. Michael Biggerstaff

---

Dr. Xuguang Wang

---

Dr. Ariel Cohen

© Copyright by MATTHEW DOUGLAS FLOURNOY 2017  
All Rights Reserved.

## **Acknowledgements**

This thesis couldn't have been completed without the help of many along the way. Thank you first to my family, Lori, Doug, Dave, and Amy, for supporting me for these past 24 years. Whether it was in the classroom, on the soccer field, or in piano lessons, thank you for constantly pushing me to do my best.

I would also like to thank my advisor, Dr. Mike Coniglio. His guidance for the past three years (even before I started graduate school) has been critical in shaping my research skills and professional goals. I am always grateful for his advice and the opportunities he has given me, both academically and in the field. I would also like to thank my other committee members, Drs. Michael Biggerstaff, Xuguang Wang, and Ariel Cohen. Special thanks are given to Ariel, who took me in as an undergraduate Hollings student and paved the way for me to begin my graduate studies here at OU.

I am also grateful for the constant support provided to me by the SoM faculty and staff and NSSL scientists. I would like to thank Keli Pirtle for her guidance in both the Hollings program and later during my graduate studies. I'd also like to thank Drs. Adam Clark and Erik Rasmussen for their support and many entertaining conversations.

Lastly, thank you to my friends, both at OU and afar. To the Krocaks - thank you for opening your home up to me and making me feel at home while I'm there. To Addison Alford, Matt Gropp, Josh Gebauer, Allie Brannan, and many others - thank you for being great friends and supporting me all these years. And lastly, thank you to Kenzie Krocak, my better half, for going through this crazy journey with me and being by my side every step of the way.

## Table of Contents

Acknowledgements .....	iv
List of Figures.....	vi
Abstract.....	xiii
Chapter 1: Introduction and Background .....	1
Mesovortices in MCSs .....	1
Tornadoes in MCSs .....	7
Chapter 2: The 5-6 July 2015 PECAN Case .....	10
Synoptic Overview .....	10
PECAN Field Deployment.....	13
Chapter 3: Numerical Simulation Configuration .....	15
Chapter 4: Simulation Results .....	18
1 km Forecasts .....	18
333 m Forecasts .....	20
Chapter 5: Summary and Discussion .....	31
References .....	39

## List of Figures

- Figure 1: Map of the damage from tornadoes (identified by “No.”), downbursts (identified by large numeral), and microbursts (identified by an “m”) on 6 August 1977. Streamlines of damage and F-scale contours are mapped. From Forbes et al. (1983)..... 51
- Figure 2: Schematic showing the formation of a pair of cyclonic and anticyclonic MVs via tilting of horizontal vorticity. The tilting agent is a downdraft, depicted by vertical arrows. Baroclinically generated horizontal vortex lines are shown in black, and the surface gust front is shown as a piped green line. The red (blue) area shows the location of the low-level cyclonic (anticyclonic) MV. From Trapp and Weisman (2003)..... 52
- Figure 3: Schematic showing the formation of a cyclonic MV via the “supercell mechanism” (e.g. tilting and stretching of near-surface horizontal and vertical vorticity transported to the surface by a downdraft). Blue and red arrows represent storm-internal and environmental airflow, respectively, and gold arrows represent low-level horizontal vortex lines. The green arrows show the location of the cyclonic MV. From Atkins and St. Laurent (2009b). ..... 53
- Figure 4: Schematic showing the formation of a cyclonic MV influenced by surface friction and a rotor. In Phase I, an outflow surge results in a vortex arch. In Phase II, tilting and stretching of frictionally generated horizontal vorticity strengthens the cyclonic member of the vortex arch. In Phase III, a second outflow surge induces rotor-like flow along the gust front. In Phase IV, the upward branch of the rotor coincides with the low-level cyclonic MV, further

intensifying it and producing a tornado-like vortex. From Schenkman et al. (2012). .....	54
Figure 5: Schematic showing the formation of an MV influenced by a descending RIJ and frictionally induced horizontal vorticity. From Xu et al. (2015). .....	55
Figure 6: Hourly snapshots of the observed 40 dBZ reflectivity contour from 0000 - 0600 UTC 6 July 2015. The positions of eight mobile radars and their baselines are shown in southeastern SD, as well as the location of the MGs. ....	56
Figure 7: Rapid Refresh model analysis of 300 mb geopotential height (contoured from 9150 m to 9750 m at 50 m intervals) and wind speed (shaded) at 0000 UTC 6 July 2015. ....	57
Figure 8: Rapid Refresh model analysis of 500 mb geopotential height (contoured), temperature (dashed from -20°C to -4°C at 2°C intervals), and vorticity (shaded) at 0000 UTC 6 July 2015.....	58
Figure 9: Environmental sounding and hodograph from the 0324 UTC MG1 launch at the location noted in Figure 6. ....	59
Figure 10: Rapid Refresh model analysis of 850 mb geopotential height (contoured from 1340 m to 1620 m at 20 m intervals) and temperature (shaded) at 0000 UTC. ....	60
Figure 11: SPC mesoanalysis of pressure (contoured in black), dewpoint temperature (shaded), temperature (contoured in red/purple), and surface wind barbs at 0000 UTC 6 July. ....	61

Figure 12: Overview of the mobile GAUS, mesonet, and radar locations at 0326 UTC overlaid with state counties and MRMS reflectivity. The enlarged “MG1” circle represents a radiosonde launch from that platform at this time (see Fig. 9). ..... 62

Figure 13: Summary of some of the observing time periods for different platforms during IOP-20 on 5-6 July 2015. Solid horizontal lines indicate continuous data collection from a certain platform during that time period (e.g. radar scanning, near-surface mesonet observations, lidar measurements, etc.), and filled circles indicate a balloon launch from a mobile mesonet, PISA, or fixed PISA at that time. .... 63

Figure 14: The nested domains used for this study. Four grids were used, with each one-way nested with its parent grid. .... 64

Figure 15: Schematic summarizing the modeling strategies used in this study. Thick, light gray horizontal arrows at the top represent the time over which each model grid was run. The black timeline is shown in the center for reference. Hourly assimilation cycles occurred on the 15 km grid from 0000 UTC July 5 - 0600 UTC July 6, 15-minute assimilation cycles occurred on the 3 km grid from 0000 - 0600 UTC July 6, and 1 km (333 m) forecasts were launched at 0300 (0345) UTC. The 15-minute 3 km analyses from 0300 - 0600 UTC are used as lateral boundary conditions for the 1 km forecasts. Periods of data collection from different platforms are indicated below and were assimilated onto the 3 km grid during the times shown by the color bars. The time of the observed tornadic mesovortex is highlighted in red. .... 65



Figure 16: Paintball plot showing the vertical vorticity contour of  $0.01 \text{ s}^{-1}$  averaged in approximately the lowest 150 m AGL for each ensemble member from 0400 - 0600 UTC, centered in SE SD. Each member is represented by a different color. Two tornado warnings issued by the Sioux Falls National Weather Service Forecast Office are also shown along with the times that they were issued and expired. .... 66

Figure 17: 1 km forecast surface reflectivity, vertical vorticity, and ground-relative wind barbs from 0430 - 0510 UTC in southeastern SD. .... 67

Figure 18: Observed analyses at 0520 UTC (courtesy of Conrad Ziegler, NSSL). Reflectivity, winds, and vertical velocity are derived using multi-Doppler analyses from multiple mobile radars. The locations and baselines of these radars are shown. Severe outflow ( $\geq 26 \text{ m s}^{-1}$ ) is highlighted with a thick, light gray line. The black box represents the domain plotted in the zoomed-in figures below. The dashed black line indicates the subjective location of the surface gust front. The strong, tornadic MV is evident (circled in blue), as well as a weakening, nontornadic MV (circled in green). .... 68

Figure 19: As in Fig. 17, except from 0425 - 0505 UTC on the 333 m forecast grid. ... 69

Figure 20: 0-1 km storm-relative helicity (SRH; shaded) and 1 km AGL vertical vorticity (contoured). Surface ground-relative wind barbs are shown, along with the subjective location of the primary gust front (dashed black line). The location of the southern (northern) MV at 0433 (0445) UTC is indicated with a green (blue) circle. .... 70

Figure 21: Partial observed sounding from MG1 at 0430 UTC south of an inflow cell.

The sonde signal was lost near 800 mb, but collected sufficient data for low-level SRH calculations. Note that the subsequent storms had a motion closer to 15 kt at 280°, so low-level SRH was likely higher than the values shown here. 71

Figure 22: Low-level hodographs obtained from the Doppler wind LIDAR (DWL)

aboard the CLAMPS platform from 0354 - 0454 UTC. Immense strengthening of winds near 1 km AGL is evident from 0354 - 0454 UTC, resulting in an environment with a significant amount of low-level SRH. The “X” in the lower right panel represents the approximate observed motion of the MVs. .... 72

Figure 23: As in Fig. 20, except with surface  $\theta_e$ -deficit and surface vertical vorticity.

The subjective positions of gust fronts and outflow boundaries at the surface are denoted with dashed, red lines. .... 73

Figure 24: As in Fig. 23, except with vertical vorticity (contoured in pink) and

horizontal vorticity near the surface (arrows). The shading represents the difference between the streamwise and crosswise components of the vorticity. Positive (green) areas represent flow that contains more streamwise than crosswise near-surface (i.e. second-lowest model level, ~30 m AGL) horizontal vorticity. The subjective locations of surface gust fronts and outflow boundaries are denoted with dashed, red lines. The storm motion used to calculate storm-relative flow is shown. .... 74

Figure 25: As in Fig. 24, except for 0-1 km AGL horizontal vorticity. The same storm

motion was used for storm-relative flow calculations. .... 75

Figure 26: Zoomed-in view of the strengthening phase of the southern (stronger) MV. 30 m AGL horizontal vorticity tilting is shown, along with 1 km AGL vertical vorticity (contoured in pink), surface reflectivity  $\geq 40$  dBZ (gray contour), and 500 m updraft (solid green line) and downdraft (dashed brown line). Arrows represent horizontal vorticity at 30 m AGL. The subjective locations of surface gust fronts and outflow boundaries are denoted with dashed, red lines. .... 76

Figure 27: As in Fig. 26, except for the northern simulated MV from 0425 - 0445 UTC. .... 77

Figure 28: Zoomed-in view of the southern MV during its development phase. 300 m AGL stretching of vertical vorticity is shaded, along with surface vertical vorticity, surface reflectivity, and 500 m AGL updraft and downdraft. Surface ground-relative wind barbs are shown. Subjective locations of surface gust fronts and outflow boundaries are denoted with dashed, red lines..... 78

Figure 29: As in Fig. 28, except for the northern simulated MV from 0425 - 0445 UTC. .... 79

Figure 30: Horizontal trace of a parcel entering the low-level MV. Heights AGL are colored along the 10-minute backward trajectory according to the color bar, and the width of the trace is proportional to the magnitude of the parcel's vertical vorticity (see the bottom right corner of the plot). Stretching  $\geq 0.0002 \text{ s}^{-2}$  at 280 m AGL and tilting  $\geq 0.000009 \text{ s}^{-2}$  at 80 m AGL at 0433 UTC are shaded in red and blue, respectively. The 40 dBZ reflectivity contour at 0433 UTC is shown as a light gray line. .... 80

Figure 31: Time-series of interpolated and integrated vertical vorticity and parcel height  
along a Lagrangian trajectory entering the low-level MV. .... 80

Figure 32: Time-series of vertical vorticity budget terms for the same parcel shown in  
Fig. 30. The inset shows a zoomed-in view of the 100-300 s timeframe, in which  
the parcel first consistently acquires positive vertical vorticity near 50 m AGL.  
..... 80

## **Abstract**

Understanding and forecasting nocturnal thunderstorms and their hazards remain elusive goals. To this end, an expansive array of fixed and mobile observing systems were deployed in the summer of 2015 for the Plains Elevated Convection At Night (PECAN) field experiment to intercept and observe nighttime atmospheric phenomena. During the night of 5 July 2015, an array of eight mobile radars and numerous ground-based surface and upper-air profiling systems directly sampled a severe mesoscale convective system (MCS) as it moved through southeastern South Dakota. The MCS was responsible for several severe wind reports, including one over 80 mph, and produced an EF-0 tornado near Dolton, SD.

In this study, observations of these phenomena from mobile radiosonde vehicles, Doppler radars, and aircraft are assimilated into an ensemble analysis and forecasting system to analyze this event. All ensemble members simulated low-level mesovortices with one in particular generating two mesovortices within the MCS in conditions very similar to those observed by the PECAN platforms. Forecasts from this member were analyzed to examine the processes leading up to the development of the vortices. In all, a supercell-like mechanism appeared responsible, with vertical vorticity initially developing via tilting in baroclinic downdrafts and then undergoing intense stretching near the surface to form the low-level mesovortices.

## **Chapter 1: Introduction and Background**

Mechanisms responsible for the development of significant low-level rotation in mesoscale convective systems (MCSs) have been studied for decades. Forbes et al. (1983) performed a case study of a particularly damaging MCS and associated mesovortices (MVs) and tornadoes that produced EF0-EF3 damage near Springfield, IL (see Figure 1). They theorized that the observed straight-line wind damage was associated with low-level mesovortices (MVs). These vortices typically reside on the meso- $\gamma$  scale (Orlanski 1975; 2-20 km) in length, extend from 1-2 km above ground level (AGL) a few kilometers into the atmosphere, and persist for no more than an hour. These features distinguish MVs from other mid-tropospheric vortices, including book-end vortices (e.g. Weisman 1993) and mesoscale convective vortices (MCVs; e.g. Menard and Fritsch 1989; Cotton et al. 1989), which are typically larger (meso- $\beta$  scale (Orlanski 1975) in length, 20-200 km) and can persist for hours (several, in the case of a MCV). MVs are also typically most intense closer to the surface (1-2 km AGL), thus explaining their capability of producing straight-line surface wind damage and, occasionally, tornadoes. This inherent severe threat associated with MVs has made them the subject of many studies, which have yielded multiple theories as to how they form and become dynamically associated with strong winds and tornadoes.

### **Mesovortices in MCSs**

MVs have long been blamed for producing severe surface winds within MCSs in observational studies (e.g. Forbes et al. 1983; Funk et al. 1999; Przybylinski et al. 2000; Atkins et al. 2004; Atkins et al. 2005; Wakimoto et al. 2006a; Schenkman et al. 2011b;

Mahale et al. 2012; Newman et al. 2012). Such MV-induced wind events tend to be localized in space and time, on the order of tens of kilometers and minutes, as opposed to derecho-type events that propagate hundreds of kilometers over several hours. Because of this, forecasting severe wind associated with MVs is a highly complex problem, and the study of both (a) synoptic conditions conducive for the development of MVs and (b) mechanisms forcing MV-genesis in MCSs remain active areas of research.

It has been shown that  $15\text{-}20\text{ m s}^{-1}$  of vertical wind shear in the lowest 5 km of the environment is conducive for the development of MVs (Weisman and Trapp 2003). Intense MVs capable of producing tornadoes are more likely when this wind shear is oriented normal to the convective line in the lowest 3 km (Schaumann and Przybylinski 2012). These values are qualitatively consistent with RKW theory (Rotunno et al. 1988), which associates strong cold-pool forced updrafts (and subsequent vertical vorticity stretching and intensification) with a balance between cold pool and low-level environmental vertical wind shear. Quasi-idealized simulations of observed MVs yielded similar results, with stronger MVs forming when low-level environmental wind shear appeared to sufficiently balance cold pool shear (Atkins et al. 2009a). In other modeling studies, Snook et al. (2011) and Schenkman et al. (2011b) found that an accurate representation of low-level environmental winds was crucial for capturing the location and intensity of MVs. Thus, strong environmental low-level vertical wind shear is conducive for MV development. While this is the case, though, the presence of this shear is not necessary nor sufficient for MV formation due to mesoscale heterogeneities and storm-generated features.

Upper-level environmental wind shear is also known to be directly related to the maintenance of MCSs, and thus has an indirect influence on the formation of MVs. Based on the simulations used by Coniglio et al. (2006), the presence of upper-level shear resulted in deep overturning and taller updrafts, even in environments with weaker low-level shear and less vertical velocity along the cold pool interface. These stronger updrafts helped maintain the MCS, thus increasing its potential over time to produce low-level MVs.

The first study investigating MCS MV formation on the mesoscale hypothesized that *shearing instability* played a role (Forbes et al. 1983). Some later studies came to the same conclusion (Przybylinski et al. 1995; Wheatley et al. 2008), showing that the release of horizontal shearing instability along a system-generated gust front served as the precursor to MV development. This was ascertained due to the quasi-regular spacing of observed cyclonic MVs (roughly 7.5 times the boundary width; Miles and Howard (1964)). Ascent within forced updrafts then stretched this vorticity, yielding a vortex with a low-level maximum in intensity. While this shearing mechanism may be important for the genesis of some MCS MVs, many have been observed to form in isolation, in cyclonic-anticyclonic couplets, or at irregular spacings along the gust front. Thus, the genesis of these MCS MVs cannot be explained solely via the shearing mechanism, and other processes must be at least partially responsible.

Another mechanism that has been shown to influence MV formation in MCSs, specifically those forming in couplets, involves the *tilting of baroclinic vorticity generated internally along the cold pool interface*. These horizontal vortex lines are subsequently tilted by an updraft or downdraft. This process has been shown in



numerical simulations to generate MV couplets along the gust front, with the orientation of the couplet dependent upon whether an updraft or downdraft serves as the tilting agent. In the case of a downdraft acting as the tilting agent, studies have revealed the downdraft to be driven either microphysically (see Figure 2; e.g. evaporative cooling, melting of hail, and/or hydrometeor loading; Bernardet and Cotton 1998; Trapp and Weisman 2003; Wheatley et al. 2008; Richter et al. 2014) or mechanically (e.g. vertical pressure perturbations; Wakimoto et al. 2006b). In the case of an updraft acting as the tilting agent (Atkins and St. Laurent 2009b), the source was determined to be enhanced convergence along the gust front due to a localized downdraft within the cold pool. The updraft was found to interact with the horizontal vorticity generated baroclinically along the cold pool/environment interface, not the initial downdraft (Atkins and St. Laurent 2009b). This process is similar to that responsible for producing counter-rotating vortices in the rear-flank downdraft region of supercells (e.g. Straka et al. 2007). Regardless, the forcing for MV couplets along an MCS gust front is not ubiquitous and differs from case to case. Environmental conditions conducive for the formation of one type of MV couplet orientation over the other are not well understood, as this process appears highly sensitive to the locations of meso- $\gamma$ -scale updrafts and downdrafts relative to the gust front.

A third mechanism by which MV formation has been shown to occur in MCSs (specifically for isolated, cyclonic MVs) is the *tilting and stretching of near-surface horizontal vorticity by an updraft*. This process differs from that responsible for the formation of MV couplets because the updraft becomes collocated with the vertical vorticity maximum, producing a single rotating updraft containing a large component of

streamwise vertical vorticity (see Figure 3). This low-level vorticity is typically generated baroclinically in association with a downdraft or along a boundary (i.e. the system gust front). The downdraft process is well outlined in Parker and Dahl (2015), in which near-surface cyclonic circulation was attained solely by flow through a region of descent. The presence of environmental streamwise vorticity and friction were found to be relatively unimportant in this process; this is notable because intense MVs can form in MCSs in the absence of environmental streamwise vorticity (Weisman and Trapp 2003). In their quasi-idealized simulations, Atkins and St. Laurent (2009b) found the downdraft mechanism to be responsible for the formation of low-level horizontal vorticity, which was then tilted and stretched to form MVs. Other case studies have found similar results involving the tilting and stretching of horizontal vorticity, but found this vorticity associated with boundaries rather than downdraft regions. In these cases, a surface boundary (e.g. a primary or secondary gust front) associated with thermally direct horizontal vorticity became collocated with a low-level updraft (Przybylinski et al. 2000; Schenkman et al. 2011b). As in the case of a downdraft, this vorticity was then tilted and stretched by the updraft to form the MV. These mechanisms and the resulting collocation of the updraft and cyclonic vorticity resemble the processes responsible for the formation of low- and mid-level mesocyclones and tornadoes in supercells (Klemp and Rotunno 1983; Rotunno et al. 1985; Davies-Jones and Brooks 1993; Trapp and Fiedler 1995; Wicker and Wilhelmson 1995; Markowski et al. 2003; Straka et al. 2007; Hirth et al. 2008; Markowski et al. 2008; Markowski et al. 2009; Mashiko et al. 2009; Lee et al. 2011; Markowski et al. 2012a,b; Marquis et al. 2012; Beck and Weiss 2013; Kosiba et al. 2013; Dahl et al. 2014; Markowski 2014;

Markowski and Richardson 2014; Schenkman et al. 2014; Dahl 2015; Markowski 2016; Marquis et al. 2016; Mashiko 2016a; Mashiko 2016b; Orf et al. 2016, Rasmussen 2016, Coffey and Parker 2017).

Another source of vorticity shown to be important for MV genesis is *surface friction*. Frictional processes modify the low-level wind and vorticity fields in convective environments, but the finding that friction may be an important *source* of vorticity for MV generation is more recent. In real-data simulations of a nocturnal MCS, Schenkman et al. (2012) concluded that both surface friction and boundary layer stability played a role in the development of an intense, low-level “rotor” (see Fig. 4). The upward branch of this rotor coincided with an intense MV and tornado-like vortex. In a similar study, Xu et al. (2015) concluded that, in addition to baroclinicity, horizontal vorticity generated by surface friction contributed significantly to the development of an MV in an MCS. Frictional effects have also recently been shown to serve as an important source of vorticity in supercellular mesocyclones and tornadoes in modelling studies (Schenkman et al. 2014; Markowski 2016; Mashiko 2016b; Roberts et al. 2016); however, Markowski and Bryan (2016) found that the use of large-eddy schemes (LESs) in convective simulations may result in boundary layers that severely underestimate turbulence, resulting in gross overestimations of near-ground horizontal vorticity when frictional effects are included. Thus, the role of surface friction as an important vorticity source in convective environments remain a relatively unexplored, active area of research.

The last feature known to be associated with MVs in MCS is the *rear-inflow jet (RIJ)*; see Figure 5). This is a relatively common feature in mature MCSs and is

frequently associated with severe wind damage at the surface. These strong winds may or may not be associated with low-level MVs, but when they are, the strongest winds are typically found to the south of the MV (Atkins et al. 2009a). This is where the motion of the system, enhanced winds in the RIJ, and internal circulation of the MV are all oriented in the same direction (Wakimoto et al. 2006a). RIJs have also been shown to be associated with the development of MVs (Schaumann and Przybylinski 2012; Atkins et al. 2005; Newman and Heinselman 2012; Xu et al. 2015). As RIJs descended toward the front of the system, enhanced convergence at the gust front resulted in stronger low-level updrafts, vorticity tilting and stretching, and more intense MVs (Atkins et al. 2005). Subsequently, strengthening MVs led to an upward directed vertical pressure perturbation gradient force, which in turn enhanced low-level updrafts, strengthening the initial MVs. This mechanism may be responsible for the intensification of MVs that are located near a RIJ (e.g. Xu et al. 2015), and in some cases, the potential for an MV to produce a tornado (Atkins et al. 2005).

### **Tornadoes in MCSs**

While nearly all violent (EF4-5) tornadoes are spawned by supercells, 18% of all tornadoes are associated with QLCSs (Trapp et al. 2005). Given the propensity of QLCSs to persist overnight, these tornadoes are more likely to occur in the late night and early morning hours than supercellular tornadoes (Trapp et al. 2005). This characteristic in combination with lead times limited to an average of five minutes (Trapp et al. 1999) can render QLCS tornadoes just as dangerous to the public as their supercellular counterparts (Ashley 2007; Ashley et al. 2008). Thus, the investigation of

low-level processes influencing tornadogenesis in QLCSs remains an active area of research.

As in the case of supercellular tornadoes, QLCS tornadogenesis appears to be directly related to the presence of a low-level MV. Atkins et al. (2004, 2005) found all tornadoes in two damaging Midwest derechos to be associated with low-level MVs. These MVs were stronger, deeper, and lasted twice as long as nontornadic MVs; this is an intriguing finding, as supercellular mesocyclones that produce tornadoes may not be significantly different from those that do not (Atkins et al. 2004). Atkins et al. (2005) also concluded that the stronger MVs associated with tornadoes may have been forced by a descending RIJ (e.g. Schaumann and Przybylinski 2012; Xu et al. 2015).

To date, nocturnal QLCS tornadogenesis has only been simulated once. In this study, Schenkman et al. (2012) used the Advanced Regional Prediction System (ARPS) to examine processes leading to tornadogenesis in a QLCS MV in central OK on 8-9 May 2007. Using a double-nested 100 m grid and three-dimensional variational data assimilation (3DVAR) on the two outer grids, they were able to reproduce a submesovortex-scale tornado-like vortex (TLV). The genesis of this TLV was associated with a strong low-level updraft and mesovortex, which produced strong convergence, tilting, and stretching/amplifying of vorticity. It was concluded that frictionally generated horizontal vorticity within a strong rotor was the primary vorticity source for TLV-genesis. This near-surface vorticity was initially crosswise but became more streamwise in response to parcels accelerating and turning cyclonically toward the low-level updraft. (This rotor resembles simulated streamwise vorticity currents, or vorticity rivers, that have recently been observed at low-levels in high-resolution

supercell simulations to the north of the mesocyclone (Orf et al. 2016, Rasmussen 2016, Coffey and Parker 2017). However, Schenkman et al. (2012) found the presence of both nocturnal stability and surface friction critical for the development of the QLCS rotor; these features were not present in the aforementioned supercell simulations.) This horizontal vorticity was then tilted and stretched by the low-level mesovortex to form the TLV. As this was a case study, the results may not be applicable to other QLCS tornadoes, and further investigation of low-level processes influencing tornadogenesis in QLCS is warranted.

This study provides an examination of the processes leading to MV-genesis and tornadogenesis in a MCS that occurred during the Plains Elevated Convection At Night (PECAN) field experiment on 5-6 July 2015. The next section features an overview of the synoptic conditions during the event as well as the PECAN assets that were deployed that night. Next, a description of the configuration used for the simulation in this study is provided. Simulation results related to both MV-genesis and tornadogenesis are described in section 4, followed by conclusions and discussions in section 5.

## **Chapter 2: The 5-6 July 2015 PECAN Case**

By 0000 UTC on 6 July 2015, a cluster of organized severe thunderstorms had developed in south-central SD. These storms grew upscale into a leading-line trailing-stratiform (LLTS) MCS and propagated eastward, producing a swath of severe wind damage and gusts above 80 knots (see Fig. 6). A second cluster of storms developed in eastern SD around 0200 UTC and propagated southeastward. These two systems merged in southeastern SD around 0400 UTC. Furthermore, a smaller, broken line of storms initiated ahead of these systems around 0330 UTC and moved to the north. This resulted in a complex of thunderstorms with both QLCS and intermittent quasi-supercellular characteristics. In this section, synoptic conditions promoting this mesoscale storm evolution are discussed, as well as the activities of PECAN field assets during the deployment.

### **Synoptic Overview**

At upper levels, a broad, positively tilted trough was present in Manitoba and Quebec with an axis of 100+ kt winds extending from Hudson Bay southwestward towards Montana (see Fig. 7). By 0000 UTC on June 6, the main jet streak rotated northeastward over Hudson Bay, while a secondary jet formed in southeastern Manitoba. While the core of this jet was ~1000 km away from the MCS in South Dakota, ageostrophic flow and upper-level divergence in the right-entrance quadrant helped create an environment in SD more supportive of organized convection. A shortwave trough north of Montana at 0000 UTC also enhanced differential cyclonic vorticity advection (DCVA) over the Dakotas, promoting synoptic-scale lift and

steepening lapse rates there. Lastly, a broad 300 mb ridge extended from western TX northward along the Front Range of the Rockies. This feature translated eastward in tandem with the trough to the north, thus increasing upper-level wind speeds, vertical wind shear, and the potential for severe thunderstorm formation over SD.

Similar features were present at mid-tropospheric levels, including a mature Canadian cyclone, upstream shortwave trough, and broad ridging to the south of the area of interest (see Fig. 8). The strong 500 mb cyclone and shortwave troughs both translated eastward during the 1800 – 0000 UTC timeframe due to CVA at that level. A mid-tropospheric front was also draped over the northern Plains, with the strongest temperature gradient located on the cyclonic-shear side of the 500 mb jet (e.g. Bluestein et al. 2015). A consequence of this environmental front was that it was relatively warm at mid-levels on the anticyclonic-shear side of the jet, which lay over SD. In this case, though, low-level temperatures and dewpoints were more than sufficient to contribute to extraordinary MLCAPE values approaching  $5000 \text{ J kg}^{-1}$  (e.g. Bluestein et al. 2015; see Fig. 9). Also, multiple 500 mb disturbances in the otherwise zonal flow were also evident over Idaho and Wyoming. Subtle differential CVA and WAA associated with these disturbances may have caused synoptic-scale rising motion and height falls in the lower half of the troposphere prior to convective development.

At 850 mb, weak temperature advections were present at 0000 UTC (see Fig. 10). Slight cooling in the 6-hour period preceding 0000 UTC (not shown) was also likely influenced by synoptically forced, adiabatic ascent, and helped to lessen the influence of any capping inversion inhibiting surface-based convection. Weak temperature advections at the 850 and 500 mb levels suggest the primary influence of



CVA on height tendencies, which is consistent with the height falls that occurred in the area between 1800 and 0000 UTC.

At the surface, general troughing was evident during the period from the Hudson Bay through the central U.S. and into New Mexico, with two main low pressure centers (see Fig. 11). The northern system in Canada was associated with strong synoptic forcing aloft; large geostrophic vorticity advection by the thermal wind yields strong vertical forcing from a Trenberth perspective (see Fig. 8), and 400-250 mb positive PV anomalies indicate isentropic ascent downstream over the surface low (not shown). Simultaneously, the southern system centered over eastern CO appeared to be driven by processes similar to those influencing the 850 mb flow patterns. Westerly flow at mid-levels drove downslope flow on the eastern slopes of the Front Range, which warmed adiabatically and conserved potential vorticity. This resulted in the development of a lee cyclone, which translated southward between 1800 UTC and 0000 UTC due to continuous downsloping and cyclonic vorticity generation on its southern flank. Lastly, a broad trough was draped between both low pressure systems; this was likely a surface reflection of temperature gradients aloft (see Figs. 8, 10), manifested at the surface as a strong frontal zone.

To the east of the southern low-pressure center, a tongue of warm, moist air was present from eastern OK northward into eastern SD. This belt of 10-20 kt flow transported moisture into southeastern SD through the day, with dewpoints reaching 25°C (see Fig. 9). This abundance of low-level moisture was a major contributor to the large amount of CAPE and low lifting condensation levels (LCLs) present on the synoptic scale. By 0000 UTC, dewpoints > 70°F were widespread along the trough axis,

where convergence had strengthened due to the deepening of the southern low pressure system. This synoptic mass adjustment also resulted in backing surface winds in southeastern SD, which contributed to 0-1 km shear around 20 kts there. While deep-layer shear was relatively small (0-6 km shear ~ 20 kts; Fig. 9), which prohibited a highly-organized system on the mesoscale, the modest low-level shear present in the veering winds was conducive for the development of MVs and tornadoes with any convection that developed, as was the case that night.

### **PECAN Field Deployment**

The PECAN field experiment occurred from 1 June – 15 July 2015 with the goal of furthering our understanding of continental, nocturnal, warm-season precipitation. This overarching goal included specific foci on four atmospheric phenomena; these included: low-level jets, bores, convective initiation, and MCSs. During most of the experiment, assets on a given night were deployed in the interest of a single focus. On July 5, a MCS was forecast to move through southern SD, and mobile field assets embarked on the twentieth intensive observing period (IOP-20) overnight from 0000 UTC – 0900 UTC 6 July 2015 to collect MCS data. These mobile assets included radars, mesonets (Straka et al. 1996) with radiosonde launching capabilities, LIDARs (Light Detection And Ranging), PISAs (PECAN Integrated Sounding Arrays), and aircraft. Data collection also occurred from fixed PISAs and stationary radars.

Figure 12 shows the locations of some of these assets relative to the approaching MCS at 0326 UTC. Eight mobile radars were arranged in a hexagon with two center points (i.e. the “Megagon”), with baselines of approximately 25-50 km. Three mobile

sounding units were deployed at the same location, each collecting near-surface mesonet data and launching radiosondes at 1-hour intervals. These launches were staggered such that vertical profiles were obtained approximately every 20 minutes as the MCS approached. Mobile mesonets collected near-surface data along transects through the storm and environment. Mobile PISAs (PECAN Integrated Sounding Arrays), including CLAMPS (Collaborative Lower Atmosphere Mobile Profiling System), were deployed in the center of the “Megagon” and collected continuous low-level profiler data from a variety of remote-sensing systems while launching radiosondes every hour. Three aircraft collected both in-situ and microphysical data during the deployment ahead of the convective lines and spiral ascents/descents within the trailing stratiform precipitation. Fixed PISA (FP) sites across Kansas and Nebraska launched radiosondes at 3-hour intervals, with continuous profiler data collection at FP1 (the ARM Central Facility near Lamont, OK) and FP2 (in Greensburg, KS). These activities are summarized in Figure 13.

For the purposes of this study, a subset of these data were assimilated into an ensemble analysis and forecasting system (described later in Chapter 3). This subset included data from six mobile radars, three WSR-88Ds (Weather Surveillance Radars), two aircraft (NOAA P-3 and NASA DC8), and radiosondes from the co-located mobile sounding units, mobile PISAs, and fixed PISAs. The six mobile radars included three DOWs (Doppler-On-Wheels), two SMART-Rs (Shared Mobile Atmospheric Research and Teaching Radars), and NOXP (NOAA X-Pol), and the three WSR-88Ds were those located in Sioux Falls, SD (KFSD), North Platte, ND (KLNK), and Aberdeen, SD (KABR).

### **Chapter 3: Numerical Simulation Configuration**

A predecessor system that has evolved into the National Severe Storms Laboratory (NSSL) Experimental Warn-on-Forecast (WoF) System for ensembles (NEWS-e) was used for this study. This system assimilates data using an Ensemble Kalman filter (EnKF; Evensen 1994; Houtekamer and Mitchell 1998; Anderson and Collins 2007) into model states created by the advanced research version of the Weather Research and Forecasting (WRF-ARW) model version 3.6.1 (Skamarock and Klemp 2008). The ensemble has 36 members that are created by using different parameterization schemes for longwave/shortwave radiation, the surface layer and heat/moisture/momentum fluxes, and turbulent mixing in the planetary boundary layer (PBL), as well as by using the initial conditions provided by 18 members of the Global Ensemble Forecast System (GEFS). The Thompson microphysics scheme was used in all members (Thompson et al. 2004). 51 vertical levels were used, with vertical grid spacing stretching from 25 m near the surface to near 780 m at the model top. Eight vertical levels were located between 0-1 km above ground level (AGL) in order to resolve atmospheric features with vertical scales of 100-200 m in that layer. A series of four nested grids were utilized, with the three inner grids nested one-way with their outer grid (see Fig. 14). Horizontal grid spacings on these grids were 15 km, 3 km, 1 km, and 333 m, respectively. Forecasts through 0600 UTC 6 July were generated on the three outermost grids for all 36 members, while only forecasts for Member 30 were run on the 333 m grid. This member was selected for higher resolution analysis because it accurately reproduced many aspects of the observed storm evolution, discussed in the next chapter. Parameterizations for this specific member included RRTMG longwave

and shortwave radiation, RUC surface physics, MYNN surface-layer physics, and a 3D TKE turbulent diffusion scheme (no planetary boundary layer scheme was used due to the high resolution of the simulation).

Figure 15 shows a schematic detailing the initialization of each grid and the data assimilation (if any) that was performed on them. The 15 km grid was initialized at 1800 UTC 4 July and allowed 6 hours of spin-up time before beginning hourly assimilation at 0000 UTC 5 July. These assimilation cycles included conventional observations from MADIS (Meteorological Assimilation Data Ingest System; Miller et al. 2007) and PECAN radiosondes. The MADIS observations include 1) mandatory and significant levels from NWS radiosondes, 2) surface data from routine aviation weather reports (METARs), marine reports (from both ships and buoys), the Oklahoma Mesonet, and mesonet observations from a variety of national networks, 3) Aircraft Meteorological Data Relay (AMDAR) reports for wind and temperature, and 4) atmospheric motion vectors (AMVs) derived from satellite observations (e.g. Coniglio et al. 2016).

At 2300 UTC, the nested 3 km grid was initialized from the 2300 UTC analysis on the 15 km grid and allowed 1 hour of spin-up time before assimilation. Assimilation on the 3 km grid then occurred every 15 minutes and included radial velocity (e.g. Snyder and Zhang 2003; Zhang et al. 2004) and reflectivity (e.g. Dowell et al. 2004; Tong and Xue 2005; Askoy et al. 2009, 2010; Yussouf and Stensrud 2010; Dowell et al. 2011; Yussouf et al. 2013) from the mobile and WSR-88D radars listed in Fig. 15 as well as radiosonde data collected during the PECAN IOP. The radar data were edited and analyzed onto a 6 km grid using a two pass Barnes scheme (Barnes 1964) before

assimilation onto the 3 km grid. Radar data editing was completed both objectively using the Py-ART (Helmus and Collis 2013) software as well as subjectively using Solo3. Radiosonde data was also manually quality controlled and thinned to 50-60 vertical levels so as not to shock the analyses with high-density vertical information. Standard errors of 5 dBZ and  $2 \text{ m s}^{-1}$  were assumed for the reflectivity and velocity observations, respectively, during the EnKF assimilation process similar to many studies that assimilate Doppler radar observations (e.g. Yussouf et al. 2013). Both of these observation types were thresholded where reflectivity was less than 10 dBZ, meaning reflectivity was assumed to be zero everywhere else to help suppress spurious storms from developing in the model. These 15-minute analyses were produced from 0000 – 0600 UTC on the 3 km grid and used as lateral boundary conditions for forecasts on the 1 km grid.

At 0300 UTC, the 1 km grid was initialized with the analysis on the 3 km grid and forecasts were generated out to 0600 UTC. Then, the 333 m grid was initialized within the 1 km grid at 0345 UTC. The 1 km forecasts were used as the initial and boundary conditions for the 333 m grid from 0345 – 0600 UTC. It is important to note that tests were performed with data assimilated onto the 1 km grid every five minutes in an attempt to constrain the analyses further toward observations on this grid. However, forecasts generated from these 1 km analyses were inferior to those generated from the downscaled 3 km analyses, with too much spurious convection generated shortly after the forecasts were initialized (not shown). This is an ongoing research problem within storm-scale assimilation systems on grids  $O(1\text{km})$  (Dustan Wheatley, personal communication).

## Chapter 4: Simulation Results

### 1 km Forecasts

Overall, the ensemble simulated this complex event well and captured the most important features, including the low-level MVs. Figure 16 shows low-level vertical vorticity  $\geq 0.01 \text{ s}^{-1}$  from all 36 members from 0400 - 0600 UTC 6 July 2015 on the 1 km grid. These vorticity swaths represent 1-3 hour forecasts, since the 1 km grid in each member was initialized at 0300 UTC. When overlaid with the KFSD tornado warnings from that night, it is evident that the ensemble succeeded in capturing the development of significant low-level rotation in two separate areas. Although these swaths did not overlap exactly with the locations of observed MVs, we believe the ensemble depicted the processes at work in the real atmosphere that resulted in the development of these two areas of low-level MVs. This is especially true for member 30, discussed next.

Figure 17 shows simulated surface fields from member 30 from 0430 - 0510 UTC, including reflectivity, vorticity, and winds, on the 1 km analysis grid. Complex storm-scale evolutions are evident, similar to what was observed. At 0430 UTC, the main broken line of storms was evident over the western part of the domain shown, which propagated toward the east-southeast. This area of convection was accompanied by a strong cold pool and attendant gust front, which is evident in the surface wind field. A secondary area of storms was located to the northeast of the broken line and propagated southward. Isolated convection was also present in the inflow sector of this convective line, similar to what was observed. Most of the inflow cells were short lived, but did modify the environmental inflow of the MCS via convective-scale downdrafts (note in Fig. 17 the divergence in the surface winds in association with these cells).

Interactions with this heterogeneous inflow were probably one of many forcings for the strong low-level MV that formed from 0440 - 0510 UTC. While this MV occurred earlier in time and farther west than the observed tornadic MV (Fig. 16), there are many spatial similarities between the observed and simulated features near the MV, as shown next. These similarities served as the motivation for our further examination of this MV in this particular ensemble member.

Figure 18 shows a multi-Doppler analysis of the event valid at 0520 UTC. The three main convective areas discussed above are evident: 1) a well-developed MCS with a large trailing stratiform region and sharp gust front, 2) the far western edge of the line of less-organized storms that were propagating southward (seen in the far northeastern part of the domain), and 3) scattered cells in the inflow sector of the two aforementioned systems. A closer inspection of the area of interest reveals the presence of large vertical vorticity along the MCS gust front in the multi-Doppler analysis, with a maximum several kilometers to the north of NOXP. This surface maximum was associated with a strong circulation at 1 km AGL as well (Fig. 18), which strengthened and became the MV that produced the EF-0 tornado at about the time of this analysis. Another area of vorticity was located just to the northwest of NOXP (best observed in the surface and 1 km AGL wind vectors); this was associated with a decaying MV. A strong RIJ was also present at this time, which was associated with a broad swath of severe outflow at the surface (winds greater than  $26 \text{ m s}^{-1}$ ). These features are well represented on the 1 km grid in member 30, except for the lifecycle of the southern MV. As will be shown, though, the lifecycle and location of the southern MV near NOXP is represented much better on the 333 m forecasts.



### 333 m Forecasts

Due to the similarities between the complex convective evolution depicted in member 30 and in observations, higher-resolution 333 m forecasts were run nested within the 1 km grid. Simulated reflectivity at the lowest model level and 1 km AGL vertical vorticity are shown in Figure 19 from 0425 - 0505 UTC. As expected, the forecasts are very similar to those on the 1 km grid except with increased resolution. The northern broken line of convection and cells developing in the inflow sector are evident, as well as a strong RIJ. This simulated RIJ is well representative of the observed RIJ with respect to its strength and location relative to the MVs, similar to those shown in Xu et al. (2015). These inflow cells induced cold downdrafts at the surface, creating a heterogeneous environment that the MCS propagates through during the time period.

On the 333 m grid though, the evolution of the two low-level meso- $\gamma$  vortices changed such that they developed and decayed separately from each other (rather than merging into one larger MV in the 1 km forecasts). The northern MV strengthened and decayed gradually, while the southern MV strengthened and decayed rapidly. The southern MV attained much higher vorticity values than the northern MV. Overall, the evolution of both vortices resembled observations much more than that in the 1 km forecasts. Compared to observations, both of the MVs appeared to form in similar locations along the main gust front, with similar interactions with the ambient air that was being modified by convective cells. Each simulated MV also resembled its observed counterpart in terms of longevity and, to an extent, intensity (although the

southern MV was not observed to be as strong as the northern MV, whereas the southern MV was stronger than the northern MV in the 333 m forecasts). These differences in peak intensity appear to be the result of some differences in the mechanisms responsible for their development, as shown next.

Storm-relative helicity (SRH) over the lowest 1 km AGL from 0425 - 0445 UTC is shown to begin highlighting some of the processes influencing the southern MV during its development phase (see Fig. 20). Values of 100-200  $\text{m}^2 \text{s}^{-2}$  were present in the inflow region of the MCS, similar to the 160  $\text{m}^2 \text{s}^{-2}$  computed from an observed sounding launched at 0430 UTC south of a convective updraft in the inflow region (Fig. 21). Large local enhancements in 0-1 km SRH were also evident in the simulation, increasing to values of 600-800  $\text{m}^2 \text{s}^{-2}$  to the northwest of the scattered inflow cells. This was physically realistic given the tendency for the inflow cells to rapidly evolve from a buoyant updraft to a rainy downdraft. Low-level SRH would be locally enhanced on the northwest side where low-level (i.e.  $\leq 1$  km AGL) environmental and outflow winds were oriented in the same direction. This region was continuously sampled by the Doppler Wind Lidar (DWL) mounted on CLAMPS for a few hours prior to the onset of convection. Velocity-Azimuth Derived (VAD) winds show a dramatic increase in low-level wind speed and veering with height about 20 minutes prior to the arrival of the convective line (Fig. 22), similar to the enhancement in low-level southerly flow in the simulations. The simulated southern MV rapidly strengthened (in terms of 1 km AGL vorticity) immediately after the MCS gust front propagated into this region of larger 0-1 km AGL SRH to the northwest of an inflow cell. This may have contributed to MV strengthening in two different ways: 1) increased surface convergence resulted in a

stronger forced updraft along the gust front, and 2) increased streamwise horizontal vorticity resulted in larger vertical vorticity as the horizontal component was tilted by the forced updraft. This led the southern MV to rapidly intensify aloft ( $\sim 1$  km AGL) slightly behind the surface gust front as low-level streamwise vorticity was tilted and advected up and over it. The southern MV then decayed rapidly as it moved into a region that had already been convectively overturned by the same inflow cell. The northern MV also moved into an area of enhanced 0-1 km SRH during its gradual development phase, although not as enhanced of a region as the southern MV encountered. This likely played a role in the intensification of the northern MV via the same process described above for the southern MV.

The heterogeneous nature of the inflow is readily seen in surface  $\theta_e$ -deficit fields, shown in Figure 23. Cold pools generated by convective downdrafts are evident, as well as swaths of air cooled by melting graupel and hail. Both MVs formed and strengthened in gradients of  $\theta_e$  at the edge of the cold pool, suggesting that the baroclinic generation and subsequent tilting of horizontal vorticity played a role in their formation. An important observation is that the southern MV rapidly strengthened prior to the arrival of very cold outflow; most of the intensification occurred in  $\theta_e$ -deficits of 0 to 2 K (0431-0435 UTC). The gradual intensification of the northern MV occurred in air with differing densities; initially, the MV strengthened in  $\theta_e$ -deficits similar to the southern MV (Fig. 23, 0431 - 0437 UTC), but rapidly encountered colder air with  $\theta_e$ -deficits approaching 10 K (0437 - 0445 UTC) as fresh outflow from another cell ahead of the gust front interacted with the inflow air. Both MVs then weakened upon being surrounded by cooler air and precipitation and cut off from their source of buoyant air,

which is a common process by which both QLCS MVs and supercellular mesocyclones are known to decay.

A further understanding of the processes influencing the development of both MVs arises by decomposing the horizontal vorticity into its streamwise and crosswise components (with respect to the storm-relative wind). The difference between these two components, shown in Figure 24, yields insight into some of the different mechanisms at work. At 0425 UTC, more crosswise than streamwise horizontal vorticity was present behind the cold pool gust front near the surface (~ 30 m AGL). This is physically realistic, given the presence of stronger winds and enhanced frictionally generated horizontal vorticity there. The orientation of the horizontal vorticity is consistent with this interpretation, given slower winds very near the surface and faster winds slightly above the surface. This near-surface vertical wind profile also accounted for the presence of slightly more crosswise than streamwise near-surface horizontal vorticity in the inflow region of the MCS. Behind the gust front, though, a convective downdraft that was spreading eastward from 0425-0437 UTC (also see Fig. 23) provided a surge of westerly momentum. This surge locally augmented the flow to become more southerly as well as low-level vorticity to become more streamwise than crosswise. This air encountered the south side of the developing southern MV, after which the MV strengthened rapidly.

Additional details regarding the evolution of the streamwise vs. crosswise nature of the low-level vorticity near the developing MVs are evident in Fig. 25. Mostly streamwise environmental vorticity is present when looking at 0-1 km AGL horizontal vorticity rather than near-surface vorticity (~ 30 m AGL); this is because the near-

surface flow is likely dominated by surface friction, and therefore mostly crosswise. This matches well with observations of the pre-convective environmental winds (see Figs. 21, 22). The gradual conversion of more-crosswise to more-streamwise vorticity via local mass-field adjustment is evident to the south of the southern MV behind the main gust front. Enhanced streamwise vorticity was also present ahead of the gust front and to the east of the northern MV for much of this period. The northern MV also rode along the primary gust front as it developed, allowing it to continue ingesting more buoyant, environmental air. On the other hand, the southern MV rapidly intensified behind the primary gust front, but then rapidly decayed due to the arrival of much colder outflow. These differences in MV location with respect to the primary gust front and areas of enhanced streamwise vorticity within the inflow yield insight into why these two MVs evolved on different timescales, discussed next.

A closer inspection of the processes leading to the rapid intensification of the southern MV is presented in Figure 26. A strong low-level updraft was forced on top of the outflow, slight behind the surface gust front around 0431 UTC as it encountered a region of enhanced inflow from the downdraft of the inflow cell discussed earlier. This enhancement is also evident in the near-surface horizontal vorticity vectors ahead of the main gust front from 0431-0435 UTC (pointing toward the WSW). Larger horizontal vorticity oriented toward the NW was also present behind the primary gust front due to a downdraft from a cell to the southwest of the developing MV. This downdraft produced large streamwise 30 m AGL horizontal vorticity relative to the east-southeast motion of the southern MV. A couple minutes later, low-level tilting of this near-ground horizontal vorticity adjacent to the updraft became large. This is consistent with

theory, given that the tilting term will be largest in gradients of  $w$ , as opposed to within the core of the updraft itself. Given the east-southeastward component of storm motion and the fact that most of the horizontal vorticity on that side of the developing vortex was streamwise, especially near the surface (see Figs. 24, 25), the updraft quickly attained cyclonic rotation and further strengthened possibly from nonlinear dynamic vertical pressure perturbations. This process occurred in space and time prior to the arrival of very cold outflow (see Fig. 23), which is an important point when compared to the northern MV.

The same analysis was performed for the northern MV while it intensified from 0425 - 0445 UTC (see Figure 27). This vortex originated in an elongated area of low-level vertical vorticity along the outflow, slightly behind the surface gust front. By 0433 UTC, a low-level updraft formed in association with a local maximum in vertical vorticity, possibly because of the enhanced convergence at the intersection of the two outflow boundaries shown in Fig. 27. This updraft persisted throughout the gradual intensification phase of the MV, but never strengthened to the updraft speeds observed in the southern MV. Weak tilting resulting in cyclonic vertical vorticity also occurred on the periphery of the low-level updraft associated with the northern MV, but it was again much weaker compared to that for the southern MV. This may have been because the southern MV was influenced by a convective downdraft that altered the MV's inflow behind the gust front to contain more streamwise vorticity over a deeper layer, whereas the northern MV encountered no such external influence in the flow near the ground.

In summary, the dynamical cause of the weaker updraft and tilting tendencies around the northern MV with respect to the southern MV is hypothesized to be twofold: 1) the weaker updraft was not as supportive of strong tilting, and 2) less *near-surface* streamwise horizontal vorticity was present in the environment to tilt and transport into a low-level updraft (Fig. 24). An inflow cell did develop ahead of the northern MV (Fig. 23), which reinforced the easterly outflow within the outflow air associated with the northern line of cells. However, it did not produce the same enhancement in near-surface streamwise horizontal vorticity that was observed in the vicinity of the southern MV behind the primary gust front. In all, the inflow of the northern MV was backed at low-levels with large amounts of SRH, but the flow *near the surface* remained mostly crosswise until the passage of the primary gust front. Thus, the northern MV did gradually intensify aloft (~1 km AGL) due to the increased 0-1 km SRH ahead of the gust front, but it did not strengthen as rapidly as the southern MV because it did not encounter a large area of mostly streamwise near-surface vorticity prior to the arrival of very cold outflow air.

To further examine the development of significant vertical vorticity near the surface (i.e. < 1 km AGL) for the southern MV, low-level vertical vorticity stretching in the vicinity of each MV was analyzed (Fig. 28). Large positive stretching tendencies began around 0429 UTC in association with the enhancement of surface vertical vorticity and the development of a low-level updraft. (It is worth noting that a positive stretching tendency means the local vertical vorticity is increasing, which either implies negative vertical vorticity lessening in magnitude, or positive vertical vorticity increasing in magnitude. In the case of this cyclonic MV, the implication is that positive

vertical vorticity is becoming larger, as supported by the pre-existing positive surface vertical vorticity). The stretching term thereafter rapidly increased through 0433 UTC as positive stretching yielded a larger vertical vorticity maximum near the ground, which further strengthened the updraft and stretching possibly via nonlinear dynamic pressure perturbations. This strengthened low-level updraft in turn strengthened the tilting process, creating a more coherent helical updraft in the lower troposphere conducive for the development of significant near-surface rotation.

This was not the case for the northern MV (see Figure 29). As previously stated, the intensification process for this vortex was much more gradual and it did not reach nearly the same intensity as the southern MV. By 0431 UTC, positive low-level stretching developed in association with the developing low-level updraft, but both were relatively weak. For the next several minutes, the magnitude of the low-level stretching fluctuated, likely in accordance with the strength of the low-level updraft. Based on the ample amount of near-surface vertical vorticity present within the developing MV, it is clear that the dynamical factor limiting intense stretching was the strength of the low-level updraft. In fact, it is worth noting that surface vertical vorticity values in both MVs at the beginning of their intensification phases were similar - around  $0.02 \text{ s}^{-1}$ . However, as seen in Fig. 23, air around the northern MV became colder after the passage of the primary gust front than that around the southern MV. Thus, even if a stronger low-level updraft developed in the northern MV as it became occluded, it would have had less time to stretch “less-cold” air before encountering the coldest outflow.



Lagrangian vorticity budget analyses along trajectories feeding into the MV yield additional information about the processes leading to the rapid formation and intensification of the southern MV. Parcel trajectories were initialized at 200 m AGL within and near the southern MV and traced backward in time for 10 minutes. Most parcels entering the low-level MV originated northward in the core of the QLCS and swept around the MV to its west and south. A parcel following this representative path is shown in Figure 30. The parcel originated in the RIJ, gradually descending from 100 m AGL to around 50 m AGL before reaching the low-level updraft and developing MV. Based on the leftward turning of the trajectory as it approached the updraft, it appears that the parcel encountered the enhanced westerly flow accompanying the downdraft behind the main gust front (see Fig. 23 at 0429 UTC). This region was characterized by more near-surface streamwise vorticity and larger horizontal vorticity (Fig. 24 at 0429 UTC), which then fed into the low-level updraft (Fig. 30). The evolution of the interpolated vs. integrated vertical vorticity and parcel height along this parcel are shown in Figure 31. The integrated vertical vorticity matches well with the simulated vertical vorticity interpolated to the location of the air parcel. A sharp increase in vertical vorticity occurred as the parcel entered the low-level updraft and MV, acquiring vorticity values near  $0.04 \text{ s}^{-1}$  at 200 m AGL.

Regarding vertical vorticity budget calculations, it is important to note that the incompressibility assumption was *not* made. Thus, as in Markowski and Richardson (2010, pp. 21), the full vorticity tendency equation, neglecting friction, is as follows:

$$\frac{d\boldsymbol{\omega}}{dt} = [(\boldsymbol{\omega} + f\mathbf{k}) \cdot \nabla]\mathbf{v} + \frac{1}{\rho^2} \nabla\rho \times \nabla p - (\boldsymbol{\omega} + f\mathbf{k})(\nabla \cdot \mathbf{v}) ,$$

which simplifies to the following when only considering the vertical component of the vorticity:

$$\frac{d(\zeta+f)}{dt} = \left( \xi \frac{dw}{dx} + \eta \frac{dw}{dy} \right) + (\zeta + f) \frac{dw}{dz} + \frac{1}{\rho^2} \left( \frac{d\rho}{dx} \frac{dp}{dy} - \frac{d\rho}{dy} \frac{dp}{dx} \right) - (\zeta + f)(\nabla \cdot \mathbf{v}) .$$

The terms on the right-hand side are as follows: 1) tilting of horizontal vorticity, 2) stretching of vertical vorticity, 3) baroclinic generation of vertical vorticity, and 4) vorticity convergence/divergence. The baroclinic term is largely negligible (as expected) but is nonzero due to the absence of the Boussinesq approximation and is therefore shown for completion. The divergence term is of the same order of magnitude as the tilting and stretching terms, and for a parcel with *cyclonic* vorticity (as is the case here) will be positive in convergent flow (i.e.  $(\nabla \cdot \mathbf{v}) < \mathbf{0}$ ) and negative in divergent flow (i.e.  $(\nabla \cdot \mathbf{v}) > \mathbf{0}$ ).

Figure 32 shows the calculation of these terms along the same backward parcel trajectory as in Figs. 30, 31. All budget terms were near zero until the parcel reached the low-level updraft near 450-500 s. This was associated with the most dramatic increase in vertical vorticity via vertical vorticity stretching and the tilting of horizontal vorticity. Air convergence also led to an increase in vertical vorticity at the updraft base (this convergence is the same process that yields a positive dynamic pressure perturbation at the updraft base, which in turn forces a stronger updraft).

Prior to reaching the updraft and being stretched, the parcel's vertical vorticity more than doubled from 300-500 s, from around  $0.004 \text{ s}^{-1}$  to near  $0.01 \text{ s}^{-1}$ . During this time period, the parcel moved through a weak downdraft region in which the tilting term gradually increased. This was in part due to the parcel encountering greater amounts of horizontal vorticity along its southeastward trajectory (see Fig. 26 at 0431

UTC), as well as processes occurring within the downdraft behind the main gust front. Given the baroclinicity present (see Fig. 23 from 0429-0433 UTC), baroclinic generation of horizontal vorticity during descent may have resulted in differential advection of the parcel, resulting in cyclonic vorticity via tilting (e.g. the slippage and “feet-first descent” described in Davies-Jones and Brooks 1993). The parcel also likely resided to the east of the strongest downdraft, experiencing the upward half of a vortex line depression and subsequently increasing cyclonic vorticity via barotropic tilting. This provided sufficient vertical vorticity to be rapidly stretched as the parcel then encountered the low-level updraft at around 500 s, forming an intense low-level MV.

## Chapter 5: Summary and Discussion

This study examined the atmospheric processes leading up to the development of two MVs within a nocturnal QLCS. This system impacted portions of southeastern SD overnight from July 5-6 2015, producing severe wind damage and a tornado near Dolton, SD. The PECAN field campaign performed an MCS mission during this time, capturing an unprecedented amount of data on the convective system and associated tornadic MV. These data, including observations from aircraft, mobile X- and C-band Doppler radars, and radiosondes, were assimilated into an ensemble analysis and forecasting system in an attempt to understand the evolution of low-level features ultimately influencing the development of the observed MVs.

The complex storm evolution was captured well by the data assimilation and ensemble of forecasts. On a forecast grid with 1 km grid spacing, all 36 members highlighted three distinct areas of convection similar to what was observed: 1) a QLCS with a broken line of convection to the west, 2) an E-W oriented region of a broken line of storms to the north that was propagating southeastward, and 3) scattered discrete cells within the inflow region of these systems. Each member also produced at least one low-level MV, though some members were more accurate in space and time with respect to observations than others. One member in particular, member 30, was selected for further, high-resolution analysis due to its qualitative ability to capture much of the observed convective evolution. These forecasts were performed on a grid with 333 m horizontal grid spacing, allowing for features down to the small end of the meso- $\gamma$  scale (2-20 km in length) to be fully resolved. The depiction of this complex convective evolution is certainly more accurate than what could be achieved using idealized

modelling systems that rely on homogeneous background environments and relatively steady-state, highly-organized convection.

Qualitatively, these forecasts were quite similar to PECAN observations. The simulation captured a strong RIJ as well as the complex convective evolution, and the subsequent heterogeneity of the environment, including multiple convective cells in the inflow region of the MCS. These cells matured rapidly and produced cold downdrafts at the surface ahead of the MCS gust front, which modulated low-level environmental conditions. Cold pools associated with these cells typically hampered the longevity of low-level MVs, while enhanced inflow created some areas *more* conducive for the formation of MVs. This simulation produced two MVs along the MCS gust front west of Dolton, SD, with a short-lived one reaching peak vorticity values much higher than the other, longer-lived MV. This is similar to observations from the event, with one relatively short-lived MV producing an EF-0 tornado and one not producing a tornado or any significant wind damage.

The stronger of the two simulated MVs developed within the MCS cold pool slightly behind the position of the surface gust front as the system encountered enhanced environmental inflow caused by an inflow cell. This inflow cell generated a strong downdraft and moderately cold outflow at the surface, with the enhanced flow outrunning the coldest air. Thus, the MCS gust front first encountered the strengthened low-level winds prior to encountering the coldest air, creating an environment quite conducive for the development of an MV. Simultaneously, a convective downdraft approached the developing MV from the southwest, enhancing near-surface horizontal vorticity that was mostly streamwise. Strong convergence near the surface promoted

forced updrafts along the gust front, which subsequently tilted and stretched ambient horizontal and vertical vorticity to MV-strength. Nonlinear dynamic pressure perturbations strengthened this updraft, which also tilted horizontal vorticity into the vertical. In all, this genesis mechanism resembles the processes responsible for the development of intense, low-level mesocyclones in discrete supercells, with the convective downdraft approaching the MV from the southwest acting as a supercell rear-flank downdraft.

An analysis of Lagrangian trajectories yields similar results. Parcels originating in the lowest 100 m of the MCS outflow accelerated horizontally toward the low-level updraft and intensifying MV. As parcels descended, small vertical vorticity appeared to be generated by slippage of the vorticity vector from the trajectory within the baroclinic downdraft. Upon arrival, vertical vorticity was rapidly increased through tilting of initially horizontal vorticity and stretching. Convergence also contributed positively beneath the updraft base, but most of the vertical vorticity within the developing MV was generated by stretching of pre-existing vertical vorticity.

The second simulated MV formed farther north, and was less intense than the southern MV but had a longer lifetime. This MV developed along the MCS outflow near the surface gust front in a zone of enhanced vertical vorticity. A low-level updraft formed near the intersection of the main MCS gust front and outflow associated with the northern E-W broken line of cells. This updraft concentrated and strengthened low-level vertical vorticity to MV-strength. The developing MV also encountered a region of enhanced low-level streamwise environmental vorticity, which contributed positively to its gradual strengthening.

An interesting result is that, although the two simulated MVs reached different peak levels of intensity, initial surface vertical vorticity values in both of them were similar (see Fig. 23). This is curious given the different evolution of the two MVs, but is consistent with recent thinking that surface characteristics between developing tornadic and nontornadic MVs (or mesocyclones in supercells) may not differ that much (e.g. Coffey and Parker 2017); rather, differences in the strength of the low-level updraft and its location relative to the surface circulation may be critical. It is how these features interact with the available near-surface vertical vorticity that dictates the potential for the development of significant low-level rotation. Coffey and Parker (2017) found a simulated tornadic supercell's mesocyclone to strengthen significantly due to: 1) the presence of a strong, *steady* low-level updraft, and 2) the *collocation* of this updraft with the surface circulation. Neither of these updraft characteristics were present in their simulated nontornadic supercell. This difference was attributed to the more streamwise nature of the vorticity of parcels entering the pre-tornadic mesocyclone (due to the environmental wind profile) as opposed to parcels entering the “pre”-nontornadic mesocyclone. Our findings here are similar, with the MV that encountered more streamwise near-surface vorticity because of an additional convective downdraft becoming stronger than the other.

This distinction is also evident when comparing the two QLCS MVs under investigation. The stronger MV encountered a region of enhanced environmental inflow that increased both the *amount* of environmental streamwise vorticity (at least in the lowest 1 km AGL) and the *ratio* of low-level streamwise to crosswise environmental vorticity (see Figs. 20 and 24). This allowed for the rapid development of an intense

low-level MV prior the arrival of heavier precipitation and colder air behind the surging gust front. The second, weaker MV also encountered a region of enhanced low-level (i.e. 0- 1 km AGL) streamwise vorticity in the environment that was ingested into the updraft near the gust front, but near-surface horizontal vorticity was mostly crosswise at this time. Vorticity near the surface became mostly streamwise only after the passage of the gust front accompanied by the coldest air. This occurred with the stronger simulated MV as well, but the outflow surrounding the southern MV initially was not nearly as cold. Thus, although a low-level updraft formed in the northern MV, it could not sufficiently lift and stretch near-surface parcels to form a stronger, potentially tornadic MV (e.g. Markowski and Richardson 2014).

These results suggest the importance of at least three internal (i.e. within the storm) characteristics: 1) the amount of surface circulation, 2) the strength/location of the low-level updraft, and 3) the buoyancy within the surface circulation. Regarding (1), the amount of surface circulation may not reveal useful information to distinguish between tornadic and nontornadic MVs. As was the case in some supercell studies, both tornadic and nontornadic mesocyclones tended to have ample surface circulation. In QLCSs, a well-defined gust front typically exists, within which there is near-surface vertical vorticity due to cyclonic shearing across the boundary. Regarding (2), the strength and location of a low-level updraft is at least partly influenced by the environmental hodograph. Both simulated MVs encountered regions of enhanced streamwise vorticity in the environment and behind the gust front, leading to the presence of at least a modest, quasi-steady low-level updraft. This updraft was collocated with the surface vorticity maximum in both cases, as would be expected



given the findings of Coffey and Parker (2017). The important difference between the two simulated MVs in this case regards (3) - the timing of the arrival of colder air behind the surging gust front. In the case of the stronger MV, interactions with enhanced streamwise vorticity behind the gust front occurred prior to the arrival of much colder outflow. This allowed for the rapid strengthening of the MV via tilting and intense low-level stretching of horizontal and vertical vorticity, respectively. In the weaker MV, these interactions occurred after the developing MV encountered colder air from scattered inflow cells and from behind the main gust front. While the MV did gradually strengthen some, this cooler local environment limited its development and potential to produce intense, concentrated near-surface circulation.

All three of these aforementioned storm-generated characteristics are currently open areas of research, especially the degree to which they may be influenced by the environment. Any such connections would be directly applicable to forecasters, since observed and forecasted environmental data are readily available in an operational setting. While all three of these characteristics are probably influenced by the environment, some are likely more sensitive than others, and some are less easily studied than others. Relationships between the strength (and recently the location relative to the surface circulation) of the storm's low-level updraft to the environmental hodograph have been revealed by theoretical, observational, and simulation studies over the past couple of decades. However, relationships between the amount of surface circulation and buoyancy in the storm's outflow to environmental conditions remain less clear. It is known that moister environments inhibit cooling process in downdrafts (i.e. evaporation and melting) making air within them more readily lifted and stretched,

but also that stronger, colder downdrafts generate more baroclinically generated horizontal vorticity and produce more surface vertical vorticity via the slippage mechanism, at least in supercells (Davies-Jones and Brooks 1993). Thus lies the “Goldilocks problem” presented in Markowski and Richardson (2014). The applicability of these inherently baroclinic processes to real supercellular mesocyclones and QLCS mesovortices has been severely limited with respect to the amount of simulation studies in the literature. This is obviously due to the lack of thermodynamic data near the surface in these sorts of convective environments - a lack that the community hopes to address in coming years. Future work involving the development of low-level rotation in MVs and mesocyclones should focus on observations of both the storm and its environment in these baroclinic regions.

From a forecasting standpoint, this work highlights the rapidly evolving nature of QLCS severe wind and tornado events. While supercellular tornadoes are associated with persistent mid-level updrafts and low-level mesocyclones, tornadoes and straight-line winds from QLCS MVs are not. In this case, complex interactions close to the surface between a well-developed RIJ, the MCS gust front, and an erratic environment created conditions conducive for significant low-level rotation in a matter of minutes. These processes may go unnoticed by the WSR-88D network because they may occur below the lowest radar scan or in between scans. The Sioux Falls, SD radar managed to capture the MV ~50 km away while it produced a tornado, but conditions evolved too rapidly for radar updates of the developing MV to provide sufficient prognostic information to forecasters. This makes forecasting these types of events exceptionally difficult. If a radar is located close enough to an event like this, these findings suggest

that tracking the locations and intersections of surface boundaries associated with the main gust front and inflow cells will be helpful for pinpointing locations for possible, short-term MV development.

With respect to this study, future work will utilize the full ensemble suite to investigate the predictability of the MVs as well as the dynamical processes at work influencing their development. We are curious to not only ascertain whether each member produced an MV, but also *how* each member produced it. We will analyze the data collected during this PECAN mission in greater detail, as well as the comparisons between these data and our simulations. These observations will include data from mobile radars, lidars, mesonets, radiosondes, interferometers, and radiometers. These analyses will complement the simulations and produce a more complete understanding of processes influencing the development of these MVs.

## References

- Anderson, J. L., and N. Collins, 2007: Scalable implementations of ensemble filter algorithms for data assimilation. *J. Atmos. Ocea. Tech.*, **24**, 1452-1463.
- Ashley, W. S., 2007: Spatial and temporal analysis of tornado fatalities in the United States: 1880–2005. *Wea. Forecasting*, **22**, 1214-1228.
- Ashley, W. S., Krmenc, A. J., and R. Schwantes, 2008: Vulnerability due to nocturnal tornadoes. *Wea. Forecasting*, **23**, 795-807.
- Aksoy, A., Dowell, D. C., and C. Snyder, 2009: A multicase comparative assessment of the ensemble Kalman filter for assimilation of radar observations. Part I: Storm-scale analyses. *Mon. Wea. Rev.*, **137**, 1805-1824.
- Aksoy, A., Dowell, D. C., and C. Snyder, 2010: A multicase comparative assessment of the ensemble Kalman filter for assimilation of radar observations. Part II: Short-range ensemble forecasts. *Mon. Wea. Rev.*, **138**, 1273-1292.
- Atkins, N. T., Arnott, J. M., Przybylinski, R. W., Wolf, R. A., and B. D. Ketcham, 2004: Vortex structure and evolution within bow echoes. Part I: Single-Doppler and damage analysis of the 29 June 1998 derecho. *Mon. Wea. Rev.*, **132**, 2224-2242.
- Atkins, N. T., Bouchard, C. S., Przybylinski, R. W., Trapp, R. J., and G. Schmocker, 2005: Damaging surface wind mechanisms within the 10 June 2003 Saint Louis bow echo during BAMEX. *Mon. Wea. Rev.*, **133**, 2275-2296.
- Atkins, N. T., and M. St. Laurent, 2009a: Bow echo mesovortices. Part I: Processes that influence their damaging potential. *Mon. Wea. Rev.*, **137**, 1497-1513.

- Atkins, N. T., and M. St. Laurent, 2009b: Bow echo mesovortices. Part II: Their genesis. *Mon. Wea. Rev.*, **137**, 1514-1532.
- Barnes, S. L., 1964: A technique for maximizing details in numerical weather map analysis. *J. App. Meteor.*, **3**, 396-409.
- Beck, J., and C. Weiss, 2013: An assessment of low-level baroclinity and vorticity within a simulated supercell. *Mon. Wea. Rev.*, **141**, 649-669.
- Bernardet, L. R., and W. R. Cotton, 1998: Multiscale evolution of a derecho-producing mesoscale convective system. *Mon. Wea. Rev.*, **126**, 2991-3015.
- Bluestein, H. B., Snyder, J. C., and J. B. Houser, 2015: A multiscale overview of the El Reno, Oklahoma, tornadic supercell of 31 May 2013. *Wea. Forecasting*, **30**, 525-552.
- Coffer, B. E., and M. D. Parker, 2017: Simulated supercells in nontornadic and tornadic VORTEX2 environments. *Mon. Wea. Rev.*, **145**, 149-180, doi:10.1175/MWR-D-16.0226.s1.
- Coniglio, M. C., Stensrud, D. J., and L. J. Wicker, 2006: Effects of upper-level shear on the structure and maintenance of strong quasi-linear mesoscale convective systems. *J. Atmos. Sci.*, **63**, 1231-1252.
- Coniglio, M. C., Hitchcock, S. M., and K. H. Knopfmeier, 2016: Impact of assimilating preconvective upsonde observations on short-term forecasts of convection observed during MPEX. *Mon. Wea. Rev.*, **144**, 4301-4325.
- Cotton, W. R., George, R. L., Wetzel, P. J., and R. L. McAnelly, 1983: A long-lived mesoscale convective complex. Part I: The mountain-generated component. *Mon. Wea. Rev.*, **111**, 1893-1918.

- Dahl, J. M., Parker, M. D., and L. J. Wicker, 2014: Imported and storm-generated near-ground vertical vorticity in a simulated supercell. *J. Atmos. Sci.*, **71**, 3027-3051.
- Dahl, J. M., 2015: Near-ground rotation in simulated supercells: On the robustness of the baroclinic mechanism. *Mon. Wea. Rev.*, **143**, 4929-4942.
- Davies-Jones, R., H. Brooks, 1993: Mesocyclogenesis from a theoretical perspective. *The Tornado: Its Structure, Dynamics, Prediction, and Hazards*, 105-114.
- Dowell, D. C., Wicker, L. J., and D. J. Stensrud, 2004: High-resolution analyses of the 8 May 2003 Oklahoma City storm. Part II: EnKF data assimilation and forecast experiments. Preprints, *22nd Conf. on Severe Local Storms*, Amer. Meteor. Soc., Hyannis, MA.
- Dowell, D. C., Wicker, L. J., and C. Snyder, 2011: Ensemble Kalman filter assimilation of radar observations of the 8 May 2003 Oklahoma City supercell: Influences of reflectivity observations on storm-scale analyses. *Mon. Wea. Rev.*, **139**, 272-294.
- Evensen, G., 1994: Sequential data assimilation with a nonlinear quasi-geostrophic model using Monte Carlo methods to forecast error statistics. *J. Geo. Res.: Oceans*, **99**, 10143-10162.
- Forbes, G. S., and R. M. Wakimoto, 1983: A concentrated outbreak of tornadoes, downbursts and microbursts, and implications regarding vortex classification. *Mon. Wea. Rev.*, **111**, 220-236.
- Funk, T. W., Darmofal, K. E., Kirkpatrick, J. D., DeWald, V. L., Przybylinski, R. W., Schmocker, G. K., and Y. J. Lin, 1999: Storm reflectivity and mesocyclone evolution associated with the 15 April 1994 squall line over Kentucky and southern Indiana. *Wea. Forecasting*, **14**, 976-993.

- Helmus, J., and S. Collis, 2016: The Python ARM Radar Toolkit (Py-ART), a Library for Working with Weather Radar Data in the Python Programming Language. *J. Open Res. Soft.*, **4**.
- Hirth, B. D., Schroeder, J. L., C. C. Weiss, 2008: Surface analysis of the rear-flank downdraft outflow in two tornadic supercells. *Mon. Wea. Rev.*, **136**, 2344-2363.
- Houtekamer, P. L., and H. L. Mitchell, 1998: Data assimilation using an ensemble Kalman filter technique. *Mon. Wea. Rev.*, **126**, 796-811.
- Klemp, J. B., R. Rotunno, 1983: A study of the tornadic region within a supercell thunderstorm. *J. Atmos. Sci.*, **40**, 359-377.
- Kosiba, K., Wurman, J., Richardson, Y., Markowski, P., Robinson, P., and J. Marquis, 2013: Genesis of the Goshen County, Wyoming, tornado on 5 June 2009 during VORTEX2. *Mon. Wea. Rev.*, **141**, 1157-1181.
- Lee, B. D., Finley, C. A., and T. M. Samaras, 2011: Surface analysis near and within the Tipton, Kansas, tornado on 29 May 2008. *Mon. Wea. Rev.*, **139**, 370-386.
- Mahale, V. N., Brotzge, J. A., and H. B. Bluestein, 2012: An analysis of vortices embedded within a quasi-linear convective system using X-band polarimetric radar. *Wea. Forecasting*, **27**, 1520-1537.
- Mansell, E. R., 2010: On sedimentation and advection in multimoment bulk microphysics. *J. Atmos. Sci.*, **67**, 3084-3094.
- Mansell, E. R., Ziegler, C. L., and E. C. Bruning, 2010: Simulated electrification of a small thunderstorm with two-moment bulk microphysics. *J. Atmos. Sci.*, **67**, 171-194.

- Markowski, P. M., Straka, J. M., and E. N. Rasmussen, 2003: Tornadogenesis resulting from the transport of circulation by a downdraft: Idealized numerical simulations. *J. Atmos. Sci.*, **60**, 795-823.
- Markowski, P., Richardson, Y., Rasmussen, E., Straka, J., Davies-Jones, R., and R. J. Trapp, 2008: Vortex lines within low-level mesocyclones obtained from pseudo-dual-Doppler radar observations. *Mon. Wea. Rev.*, **136**, 3513-3535.
- Markowski, P. M., and Y. P. Richardson, 2009: Tornadogenesis: Our current understanding, forecasting considerations, and questions to guide future research. *Atm. Res.*, **93**, 3-10.
- Markowski, P., Richardson, Y., Marquis, J., Wurman, J., Kosiba, K., Robinson, P., Dowell, D., Rasmussen, E., and R. Davies-Jones, 2012a: The pretornadic phase of the Goshen County, Wyoming, supercell of 5 June 2009 intercepted by VORTEX2. Part I: Evolution of kinematic and surface thermodynamic fields. *Mon. Wea. Rev.*, **140**, 2887-2915.
- Markowski, P., Richardson, Y., Marquis, J., Davies-Jones, R., Wurman, J., Kosiba, K., Robinson, P., Rasmussen, E., and D. Dowell, 2012b: The pretornadic phase of the Goshen County, Wyoming, supercell of 5 June 2009 intercepted by VORTEX2. Part II: Intensification of low-level rotation. *Mon. Wea. Rev.*, **140**, 2916-2938.
- Markowski, P., Richardson, Y., and G. Bryan, 2014: The origins of vortex sheets in a simulated supercell thunderstorm. *Mon. Wea. Rev.*, **142**, 3944-3954.



- Markowski, P. M., and Y. P. Richardson, 2014: The influence of environmental low-level shear and cold pools on tornadogenesis: Insights from idealized simulations. *J. Atmos. Sci.*, **71**, 243-275.
- Markowski, P. M., 2016: An Idealized Numerical Simulation Investigation of the Effects of Surface Drag on the Development of Near-Surface Vertical Vorticity in Supercell Thunderstorms. *J. Atmos. Sci.*, **73**, 4349-4385.
- Markowski, P. M., and G. H. Bryan, 2016: LES of laminar flow in the PBL: a potential problem for convective storm simulations. *Mon. Wea. Rev.*, **144**, 1841-1850.
- Marquis, J., Richardson, Y., Markowski, P., Dowell, D., and J. Wurman, 2012: Tornado maintenance investigated with high-resolution dual-Doppler and EnKF analysis. *Mon. Wea. Rev.*, **140**, 3-27.
- Marquis, J., Richardson, Y., Markowski, P., Wurman, J., Kosiba, K., and P. Robinson, 2016: An Investigation of the Goshen County, Wyoming, Tornadic Supercell of 5 June 2009 Using EnKF Assimilation of Mobile Mesonet and Radar Observations Collected during VORTEX2. Part II: Mesocyclone-Scale Processes Affecting Tornado Formation, Maintenance, and Decay. *Mon. Wea. Rev.*, **144**, 3441-3463.
- Mashiko, W., Niino, H., and T. Kato, 2009: Numerical simulation of tornadogenesis in an outer-rainband minisupercell of Typhoon Shanshan on 17 September 2006. *Mon. Wea. Rev.*, **137**, 4238-4260.
- Mashiko, W., 2016a: A numerical study of the 6 May 2012 Tsukuba City supercell tornado. Part I: Vorticity sources of low-level and midlevel mesocyclones. *Mon. Wea. Rev.*, **144**, 1069-1092.

- Mashiko, W., 2016b: A Numerical Study of the 6 May 2012 Tsukuba City Supercell Tornado. Part II: Mechanisms of Tornadogenesis. *Mon. Wea. Rev.*, **144**, 3077-3098.
- Menard, R. D., and J. M. Fritsch, 1989: A mesoscale convective complex-generated inertially stable warm core vortex. *Mon. Wea. Rev.*, **117**, 1237-1261.
- Miles, J. W., and L. N. Howard, 1964: Note on a heterogeneous shear flow. *J. Fluid Mech.*, **20**, 331-336.
- Miller, P. A., Barth, M., Benjamin, L., Artz, R., and W. Pendergrass, 2007: MADIS support for UrbaNet. Preprints, *14th Symp. on Meteorological Observations and Instrumentation*, San Antonio, TX, Amer. Meteor. Soc.
- Newman, J. F., & P. L. Heinselman, 2012: Evolution of a quasi-linear convective system sampled by phased array radar. *Mon. Wea. Rev.*, **140**, 3467-3486.
- Orf, L., Wilhelmson, R., Lee, B., Finley, C., and A. Houston, 2016: Evolution of a long-track violent tornado within a simulated supercell. *Bull. Amer. Met. Soc.*, 45-68.
- Orlanski, I., 1975: A rational subdivision of scales for atmospheric processes. *Bull. Amer. Meteor. Soc.*, **56**, 527-530.
- Parker, M. D., 2014: Composite VORTEX2 supercell environments from near-storm soundings. *Mon. Wea. Rev.*, **142**, 508-529, doi:10.1175/MWR-D-13-00167.1.
- Parker, M. D., and J. M. Dahl, 2015: Production of near-surface vertical vorticity by idealized downdrafts. *Mon. Wea. Rev.*, **143**, 2795-2816.
- Przybylinski, R. W., 1995: The bow echo: Observations, numerical simulations, and severe weather detection methods. *Wea. Forecasting*, **10**, 203-218.

- Pryzbylinski, R. W., Schmocker, G. K., and Y. J. Lin, 2000: A study of storm and vortex morphology during the ‘intensifying stage’ of severe wind mesoscale convective systems. Preprints, *20th Conf. on Severe Local Storms*, Orlando, FL, Amer. Meteor. Soc., (pp. 173-176).
- Rasmussen, E. N., 2017: Some aspects of a simulated vorticity river and associated tornado cyclone genesis. *In review*.
- Richter, H., Peter, J., and S. Collis, 2014: Analysis of a destructive wind storm on 16 November 2008 in Brisbane, Australia. *Mon. Wea. Rev.*, **142**, 3038-3060.
- Roberts, B., Xue, M., Schenkman, A. D., and D. T. Dawson, 2016: The role of surface drag in tornadogenesis within an idealized supercell simulation. *J. Atmos. Sci.*, **73**, 3371-3395.
- Rotunno, R., and J. Klemp, 1985: On the rotation and propagation of simulated supercell thunderstorms. *J. Atmos. Sci.*, **42**, 271-292.
- Rotunno, R., Klemp, J. B., and M. L. Weisman, 1988: A theory for strong, long-lived squall lines. *J. Atmos. Sci.*, **45**, 463-485.
- Schaumann, J. S., and R. W. Przybylinski, 2012: Operational application of 0-3 km bulk shear vectors in assessing QLCS mesovortex and tornado potential. Preprints, *26th Conf. on Severe Local Storms*, Nashville, TN, Amer. Met. Soc., (pp. 1-25).
- Schenkman, A. D., Xue, M., Shapiro, A., Brewster, K., & J. Gao, 2011a: The analysis and prediction of the 8–9 May 2007 Oklahoma tornadic mesoscale convective system by assimilating WSR-88D and CASA radar data using 3DVAR. *Mon. Wea. Rev.*, **139**, 224-246.

- Schenkman, A. D., Xue, M., Shapiro, A., Brewster, K., and J. Gao, 2011b: Impact of CASA radar and Oklahoma Mesonet data assimilation on the analysis and prediction of tornadic mesovortices in an MCS. *Mon. Wea. Rev.*, **139**, 3422-3445.
- Schenkman, A. D., Xue, M., and A. Shapiro, 2012: Tornadogenesis in a simulated mesovortex within a mesoscale convective system. *J. Atmos. Sci.*, **69**, 3372-3390.
- Schenkman, A. D., Xue, M., and M. Hu, 2014: Tornadogenesis in a high-resolution simulation of the 8 May 2003 Oklahoma City supercell. *J. Atmos. Sci.*, **71**, 130-154.
- Skamarock, W. C., and J. B. Klemp, 2008: A time-split nonhydrostatic atmospheric model for weather research and forecasting applications. *J. Comp. Phys.*, **227**, 3465-3485.
- Snook, N., Xue, M., and Y. Jung, 2011: Analysis of a tornadic mesoscale convective vortex based on ensemble Kalman filter assimilation of CASA X-band and WSR-88D radar data. *Mon. Wea. Rev.*, **139**, 3446-3468.
- Snyder, C., and F. Zhang, 2003: Assimilation of simulated Doppler radar observations with an ensemble Kalman filter. *Mon. Wea. Rev.*, **131**, 1663-1677.
- Straka, J. M., Rasmussen, E. N., and S. E. Fredrickson, 1996: A mobile mesonet for finescale meteorological observations. *J. Atm. Ocea. Tech.*, **13**, 921-936.
- Straka, J. M., Rasmussen, E. N., Davies-Jones, R. P., and P. M. Markowski, 2007: An observational and idealized numerical examination of low-level counter-rotating

- vortices in the rear flank of supercells. *Electron. J. Severe Storms Meteor*, **2**, 1-22.
- Thompson, G., Rasmussen, R. M., and K. Manning, 2004: Explicit forecasts of winter precipitation using an improved bulk microphysics scheme. Part I: description of and sensitivity analysis. *Mon. Wea. Rev.*, **132**, 519-542.
- Tong, M., and M. Xue, 2005: Ensemble Kalman filter assimilation of Doppler radar data with a compressible nonhydrostatic model: OSS experiments. *Mon. Wea. Rev.*, **133**, 1789-1807.
- Trapp, R. J., and B. H. Fiedler, 1995: Tornado-like vortexgenesis in a simplified numerical model. *J. Atmos. Sci.*, **52**, 3757-3778.
- Trapp, R. J., Mitchell, E. D., Tipton, G. A., Effertz, D. W., Watson, A. I., Andra Jr, D. L., and M. A. Magsig, 1999: Descending and nondescending tornadic vortex signatures detected by WSR-88Ds. *Wea. Forecasting*, **14**, 625-639.
- Trapp, R. J., and M. L. Weisman, 2003: Low-level mesovortices within squall lines and bow echoes. Part II: Their genesis and implications. *Mon. Wea. Rev.*, **131**, 2804-2823.
- Trapp, R. J., Tessendorf, S. A., Godfrey, E. S., and H. E. Brooks, 2005: Tornadoes from squall lines and bow echoes. Part I: Climatological distribution. *Wea. Forecasting*, **20**, 23-34.
- Wakimoto, R. M., Murphey, H. V., Nester, A., Jorgensen, D. P., and N. T. Atkins, 2006a: High winds generated by bow echoes. Part I: Overview of the Omaha bow echo 5 July 2003 storm during BAMEX. *Mon. Wea. Rev.*, **134**, 2793-2812.

- Wakimoto, R. M., Murphey, H. V., Davis, C. A., and N. T. Atkins, 2006b: High winds generated by bow echoes. Part II: The relationship between the mesovortices and damaging straight-line winds. *Mon. Wea. Rev.*, **134**, 2813-2829.
- Weisman, M. L., 1993: The genesis of severe, long-lived bow echoes. *J. Atmos. Sci.*, **50**, 645-670.
- Weisman, M. L., & R. J. Trapp, 2003: Low-level mesovortices within squall lines and bow echoes. Part I: Overview and dependence on environmental shear. *Mon. Wea. Rev.*, **131**, 2779-2803.
- Wheatley, D. M., and R. J. Trapp, 2008: The effect of mesoscale heterogeneity on the genesis and structure of mesovortices within quasi-linear convective systems. *Mon. Wea. Rev.*, **136**, 4220-4241.
- Wicker, L. J., and R. B. Wilhelmson, 1995: Simulation and analysis of tornado development and decay within a three-dimensional supercell thunderstorm. *J. Atmos. Sci.*, **52**, 2675-2703.
- Xu, X., Xue, M., and Y. Wang, 2015: The genesis of mesovortices within a real-data simulation of a bow echo system. *J. Atmos. Sci.*, **72**, 1963-1986.
- Yussouf, N., and D. J. Stensrud, 2010: Impact of phased-array radar observations over a short assimilation period: Observing system simulation experiments using an ensemble Kalman filter. *Mon. Wea. Rev.*, **138**, 517-538.
- Yussouf, N., Gao, J., Stensrud, D. J., and G. Ge, 2013: The impact of mesoscale environmental uncertainty on the prediction of a tornadic supercell storm using ensemble data assimilation approach. *Adv. Met.*, 2013.

Zhang, F., Snyder, C., and J. Sun, 2004: Impacts of initial estimate and observation availability on convective-scale data assimilation with an ensemble Kalman filter. *Mon. Wea. Rev.*, **132**, 1238-1253.

Ziegler, C. L., 1985: Retrieval of thermal and microphysical variables in observed convective storms. Part 1: Model development and preliminary testing. *J. Atmos. Sci.*, **42**, 1487-1509.

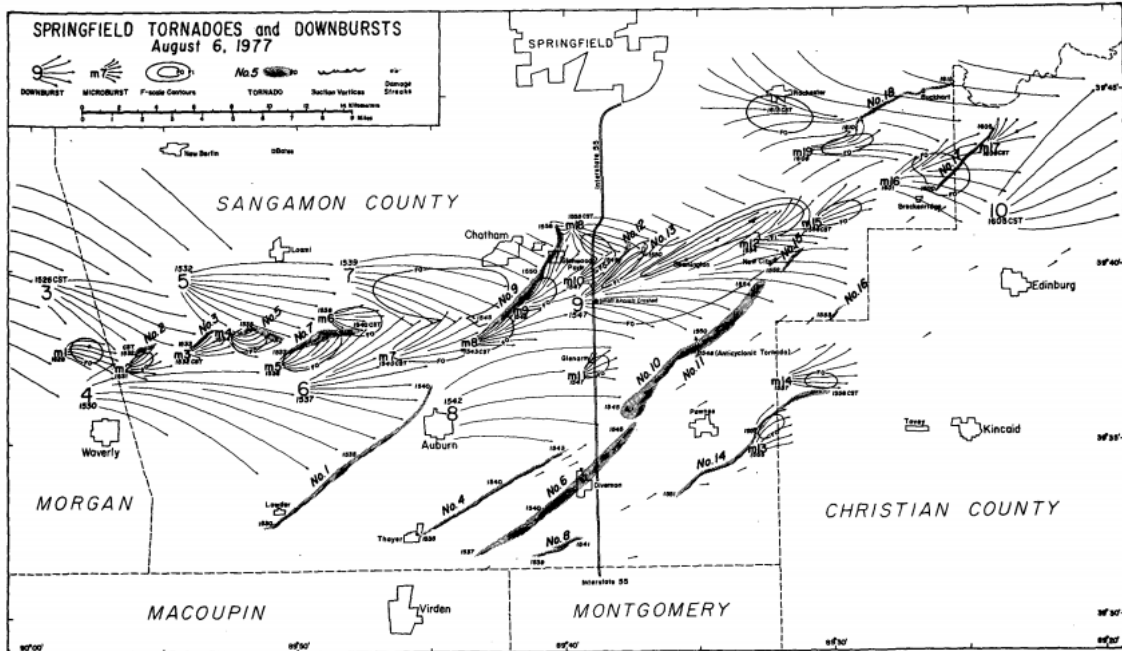


**Figure 1:** Map of the damage from tornadoes (identified by “No.”), downbursts (identified by large numeral), and microbursts (identified by an “m”) on 6 August 1977. Streamlines of damage and F-scale contours are mapped. From Forbes et al. (1983).



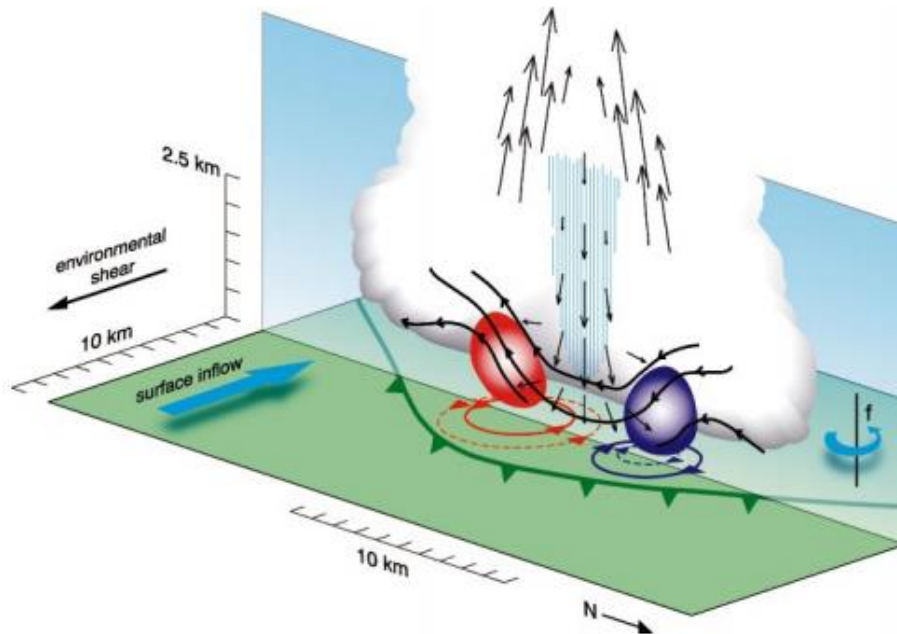


**Figure 2:** Schematic showing the formation of a pair of cyclonic and anticyclonic MVs via tilting of horizontal vorticity. The tilting agent is a downdraft, depicted by vertical arrows. Baroclinically generated horizontal vortex lines are shown in black, and the surface gust front is shown as a piped green line. The red (blue) area shows the location of the low-level cyclonic (anticyclonic) MV. From Trapp and Weisman (2003).

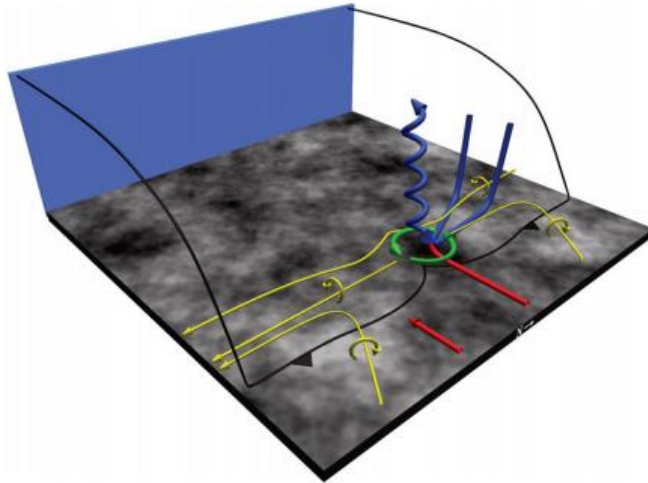


**Figure 3:** Schematic showing the formation of a cyclonic MV via the “supercell mechanism” (e.g. tilting and stretching of near-surface horizontal and vertical vorticity transported to the surface by a downdraft). Blue and red arrows represent storm-internal and environmental airflow, respectively, and gold arrows represent low-level horizontal vortex lines. The green arrows show the location of the cyclonic MV. From Atkins and St. Laurent (2009b).

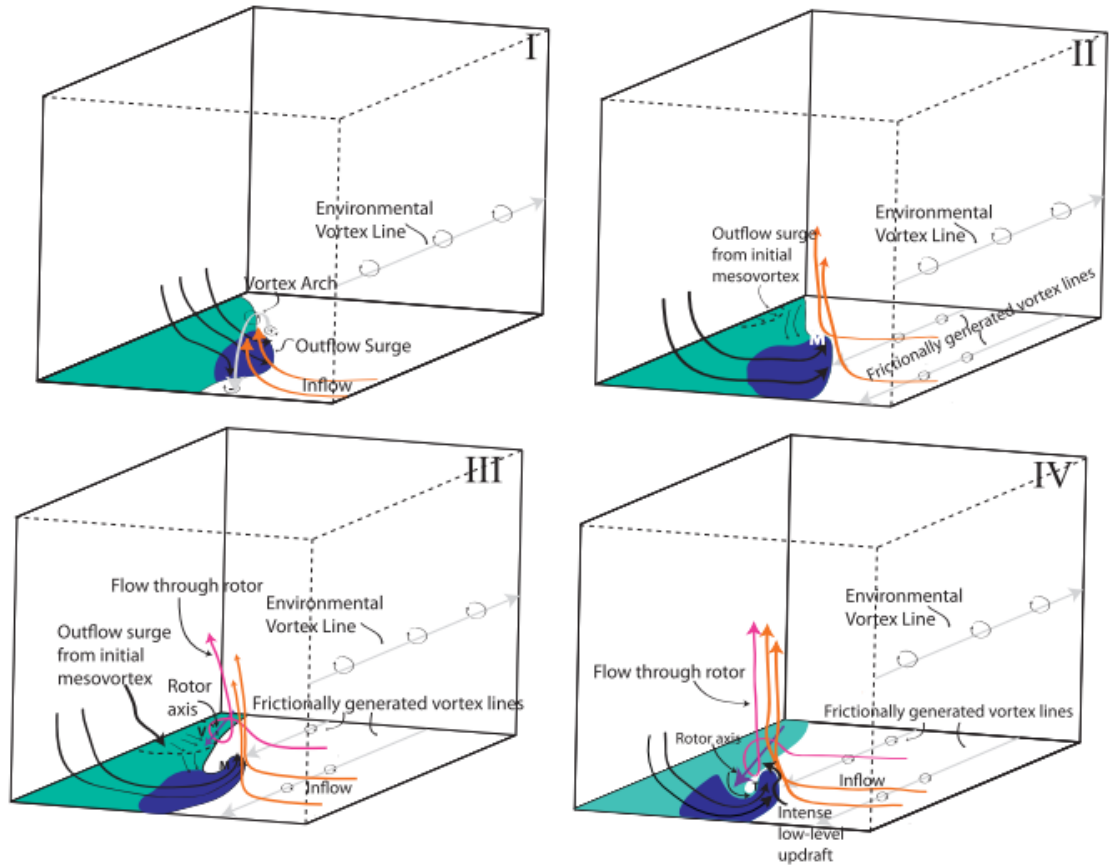


**Figure 4:** Schematic showing the formation of a cyclonic MV influenced by surface friction and a rotor. In Phase I, an outflow surge results in a vortex arch. In Phase II, tilting and stretching of frictionally generated horizontal vorticity strengthens the cyclonic member of the vortex arch. In Phase III, a second outflow surge induces rotor-like flow along the gust front. In Phase IV, the upward branch of the rotor coincides with the low-level cyclonic MV, further intensifying it and producing a tornado-like vortex. From Schenkman et al. (2012).

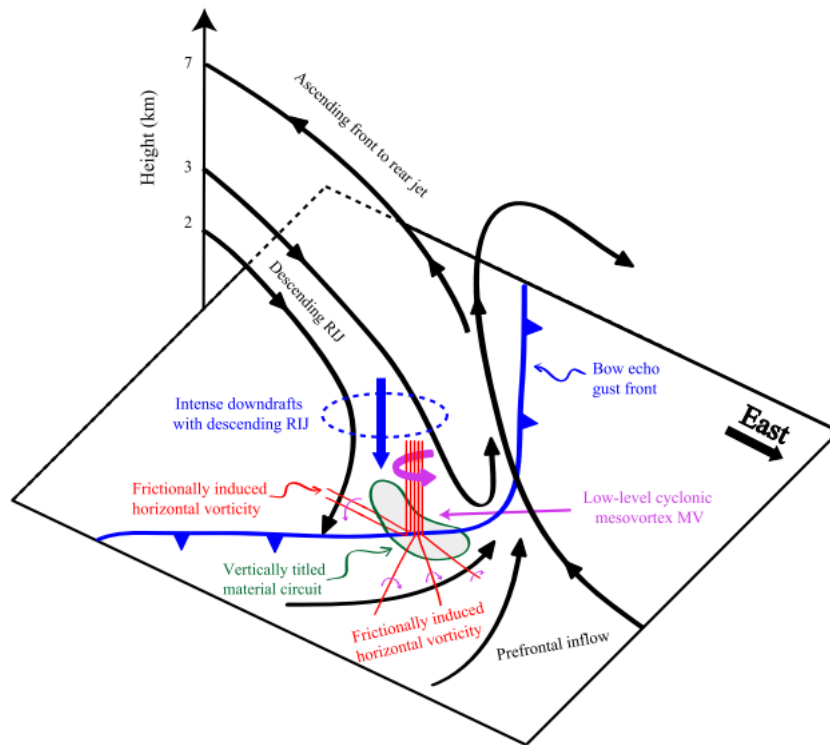


**Figure 5:** Schematic showing the formation of an MV influenced by a descending RIJ and frictionally induced horizontal vorticity. From Xu et al. (2015).

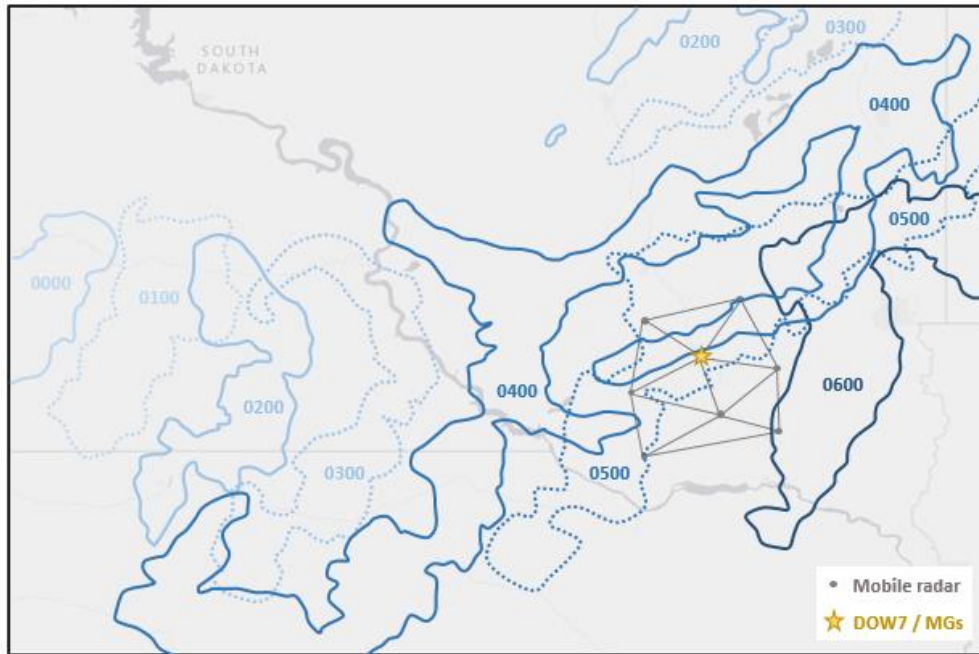


**Figure 6:** Hourly snapshots of the observed 40 dBZ reflectivity contour from 0000 - 0600 UTC 6 July 2015. The positions of eight mobile radars and their baselines are shown in southeastern SD, as well as the location of the MRGs.

## 0000 UTC 300mb Geopotential Height and Wind

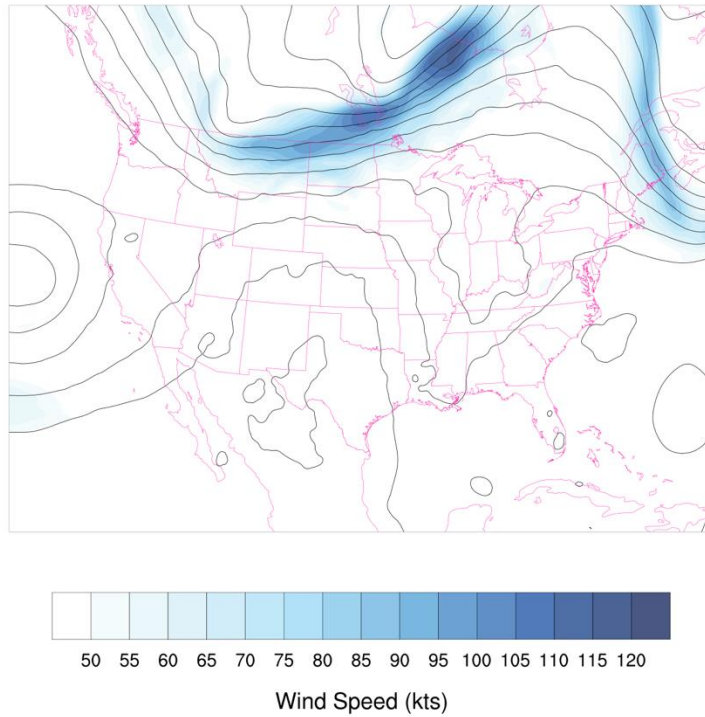
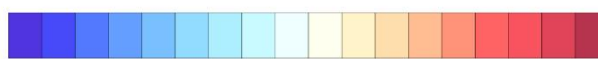
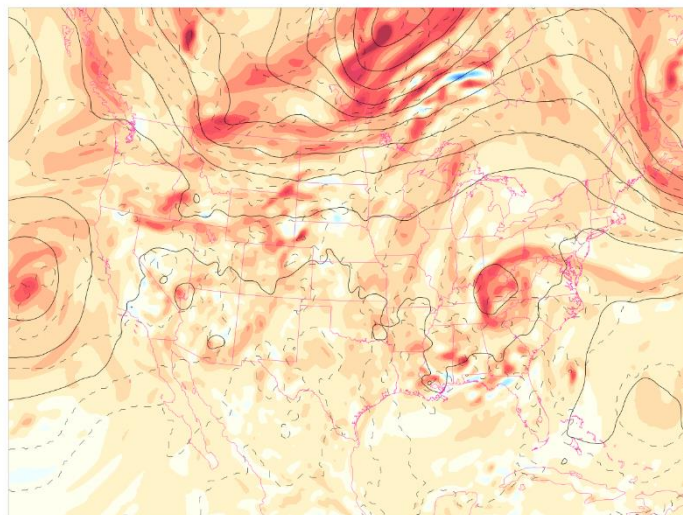


**Figure 7:** Rapid Refresh model analysis of 300 mb geopotential height (contoured from 9150 m to 9750 m at 50 m intervals) and wind speed (shaded) at 0000 UTC 6 July 2015.

### 0000 UTC 500mb Fields



-3.2 -2.4 -1.6 -0.8 0 0.8 1.6 2.4 3.2

Vorticity ( $10^{-4} \text{ s}^{-1}$ )

**Figure 8:** Rapid Refresh model analysis of 500 mb geopotential height (contoured), temperature (dashed from  $-20^{\circ}\text{C}$  to  $-4^{\circ}\text{C}$  at  $2^{\circ}\text{C}$  intervals), and vorticity (shaded) at 0000 UTC 6 July 2015.

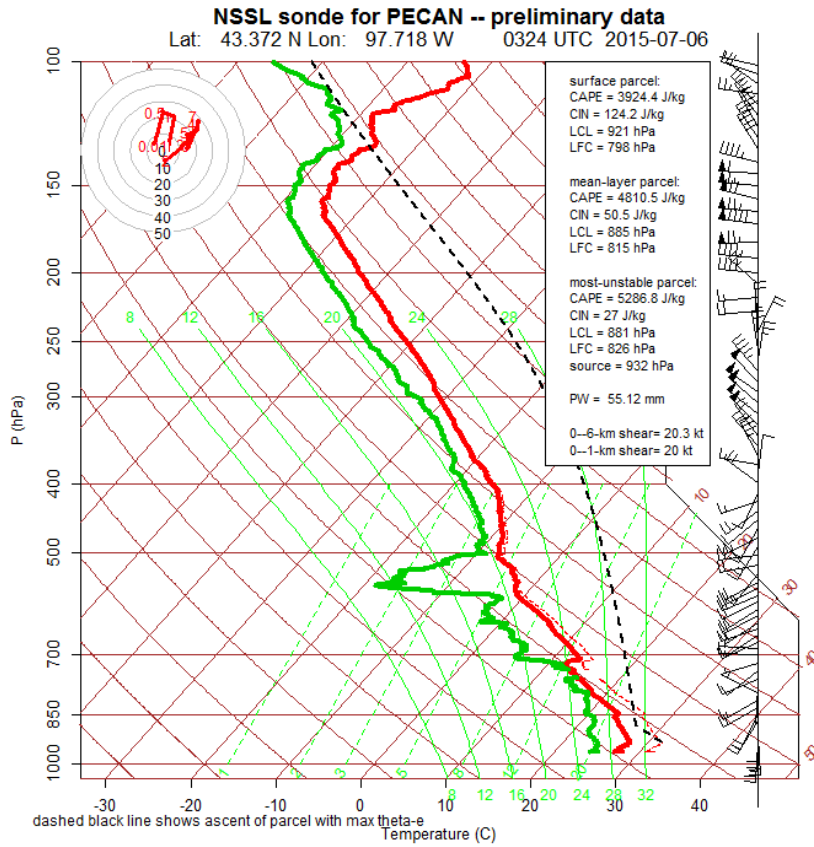


**Figure 9:** Environmental sounding and hodograph from the 0324 UTC MG1 launch at the location noted in Figure 6.



### 0000 UTC 850mb Geopotential Height and Temperature

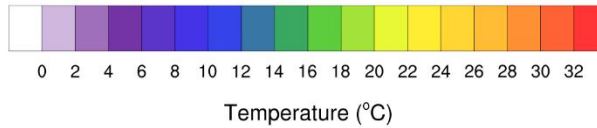
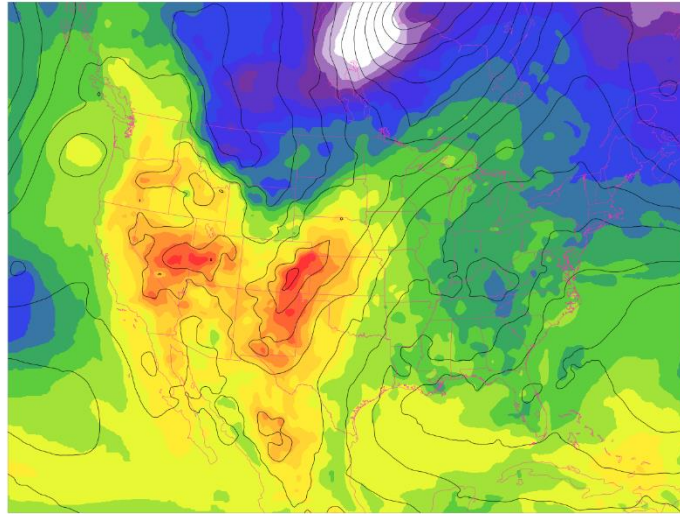


**Figure 10:** Rapid Refresh model analysis of 850 mb geopotential height (contoured from 1340 m to 1620 m at 20 m intervals) and temperature (shaded) at 0000 UTC.

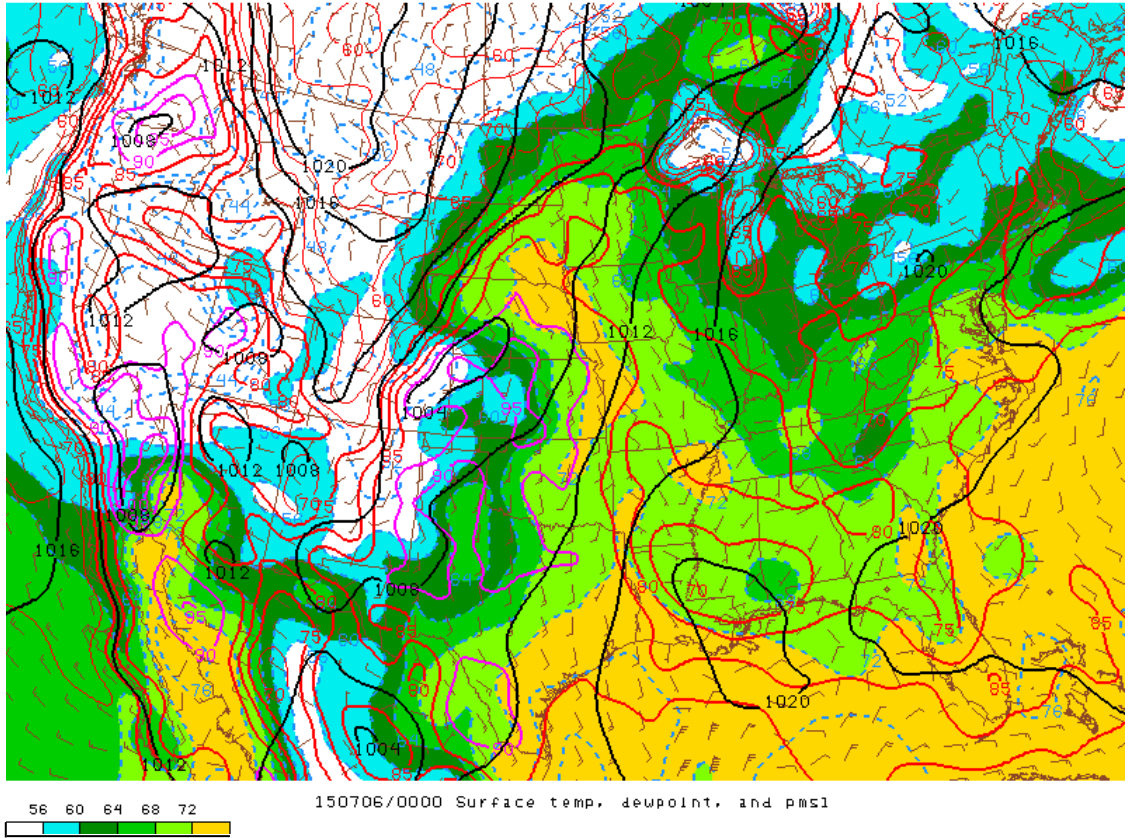


**Figure 11:** SPC mesoanalysis of pressure (contoured in black), dewpoint temperature (shaded), temperature (contoured in red/purple), and surface wind barbs at 0000 UTC 6 July.

July 6 032640z

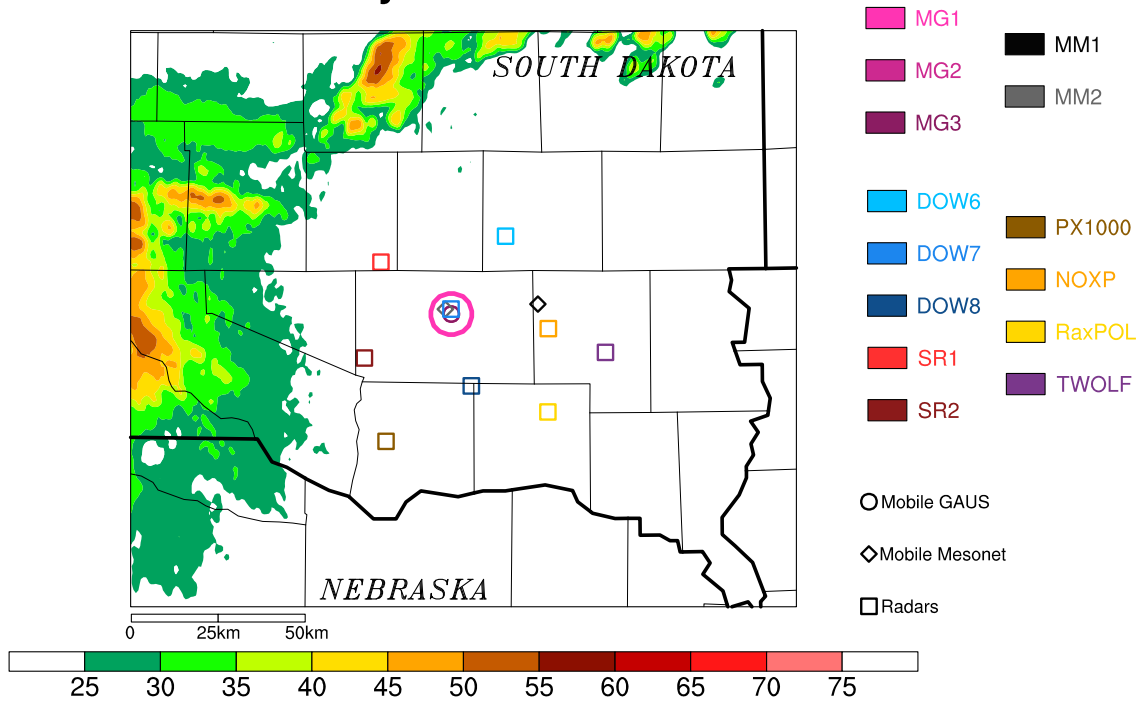


**Figure 12:** Overview of the mobile GAUS, mesonet, and radar locations at 0326 UTC overlaid with state counties and MRMS reflectivity. The enlarged “MG1” circle represents a radiosonde launch from that platform at this time (see Fig. 9).

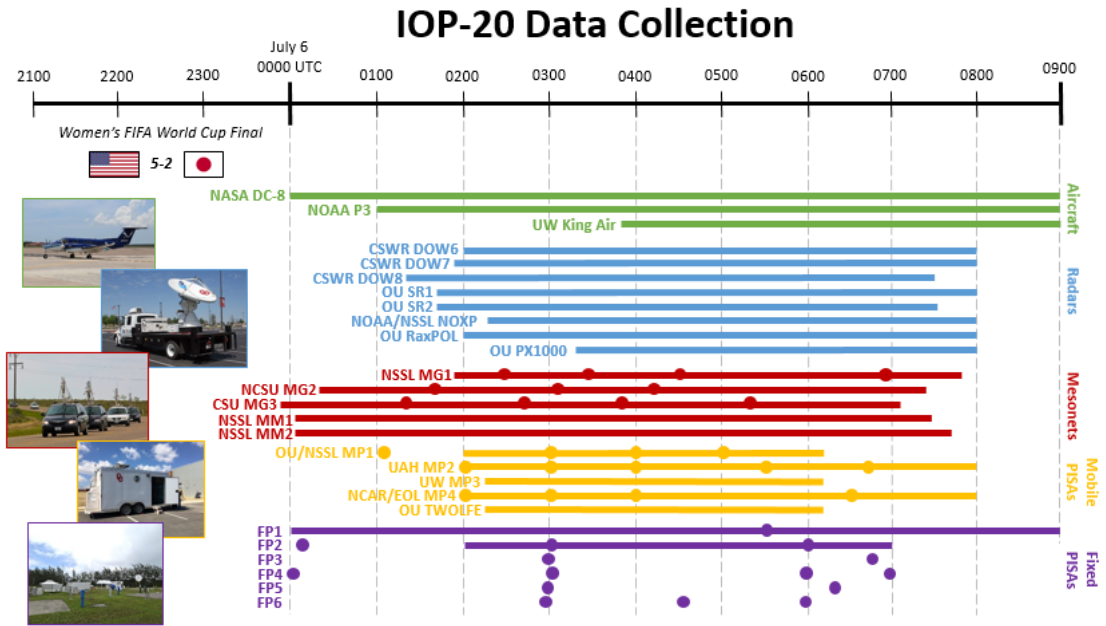


**Figure 13:** Summary of some of the observing time periods for different platforms during IOP-20 on 5-6 July 2015. Solid horizontal lines indicate continuous data collection from a certain platform during that time period (e.g. radar scanning, near-surface mesonet observations, lidar measurements, etc.), and filled circles indicate a balloon launch from a mobile mesonet, PISA, or fixed PISA at that time.

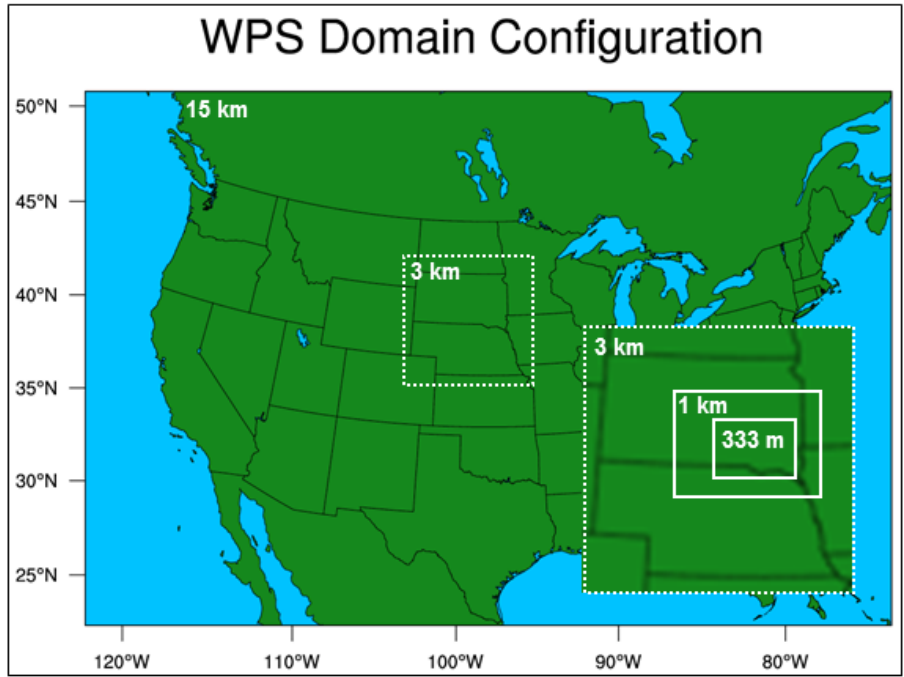


**Figure 14:** The nested domains used for this study. Four grids were used, with each one-way nested with its parent grid.

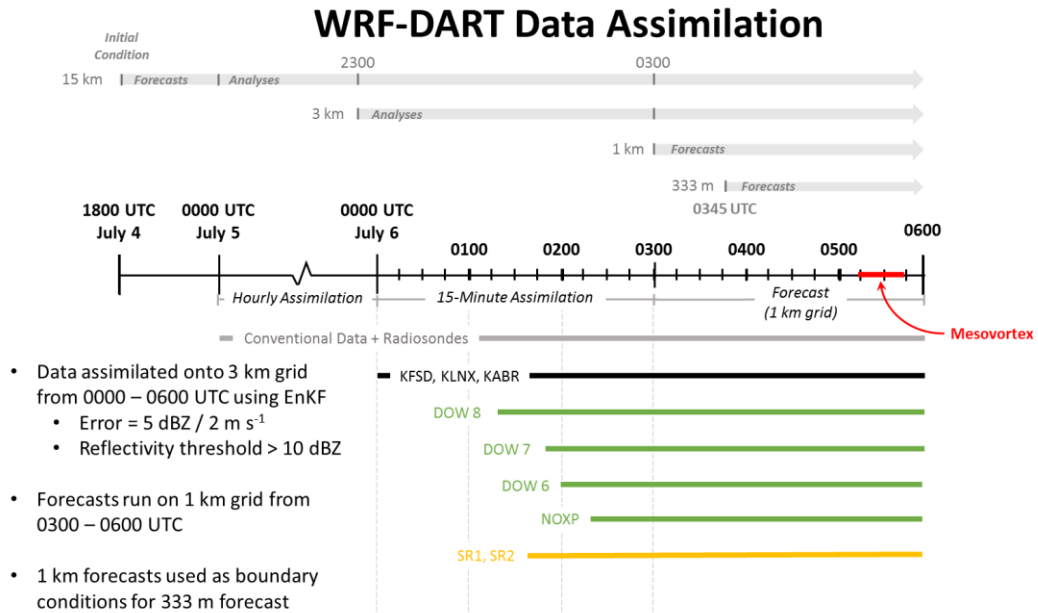


**Figure 15:** Schematic summarizing the modeling strategies used in this study. Thick, light gray horizontal arrows at the top represent the time over which each model grid was run. The black timeline is shown in the center for reference. Hourly assimilation cycles occurred on the 15 km grid from 0000 UTC July 5 - 0600 UTC July 6, 15-minute assimilation cycles occurred on the 3 km grid from 0000 - 0600 UTC July 6, and 1 km (333 m) forecasts were launched at 0300 (0345) UTC. The 15-minute 3 km analyses from 0300 - 0600 UTC are used as lateral boundary conditions for the 1 km forecasts. Periods of data collection from different platforms are indicated below and were assimilated onto the 3 km grid during the times shown by the color bars. The time of the observed tornadic mesovortex is highlighted in red.

**1-3 hour Forecast Ensemble Low-level Vorticity Swaths (0400 – 0600 UTC)**

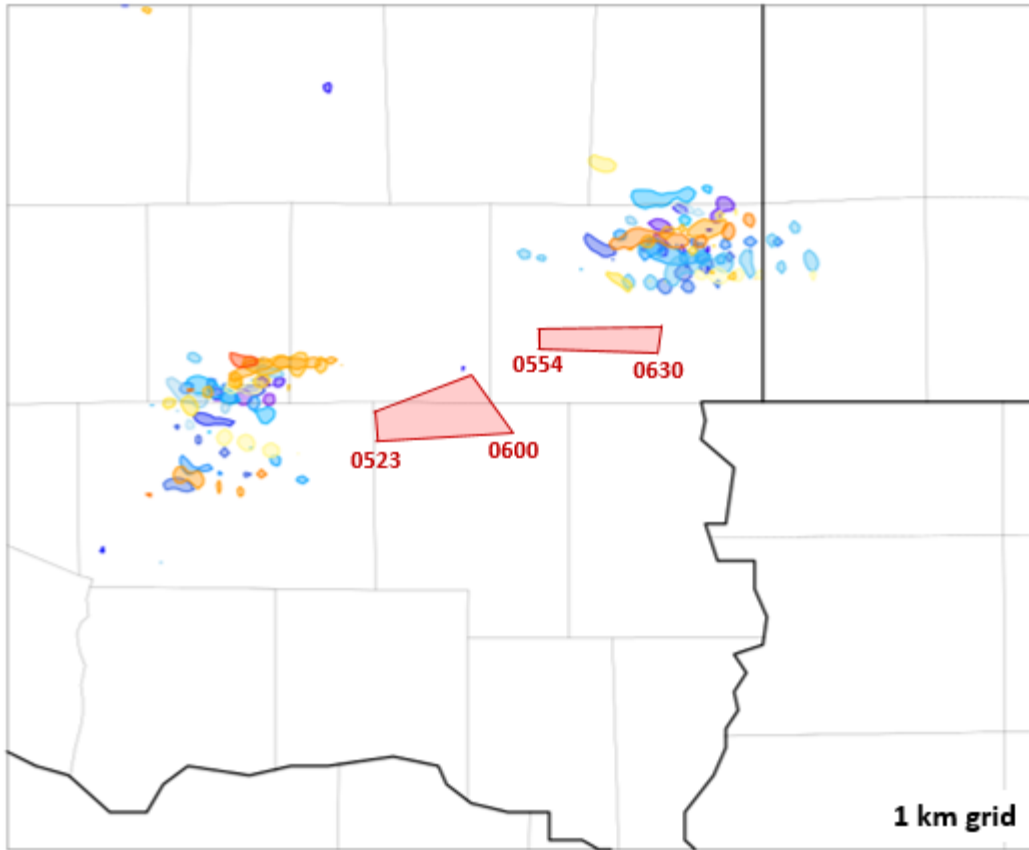


**Figure 16:** Paintball plot showing the vertical vorticity contour of  $0.01 \text{ s}^{-1}$  averaged in approximately the lowest 150 m AGL for each ensemble member from 0400 - 0600 UTC, centered in SE SD. Each member is represented by a different color. Two tornado warnings issued by the Sioux Falls National Weather Service Forecast Office are also shown along with the times that they were issued and expired.

## Surface Reflectivity and Vertical Vorticity

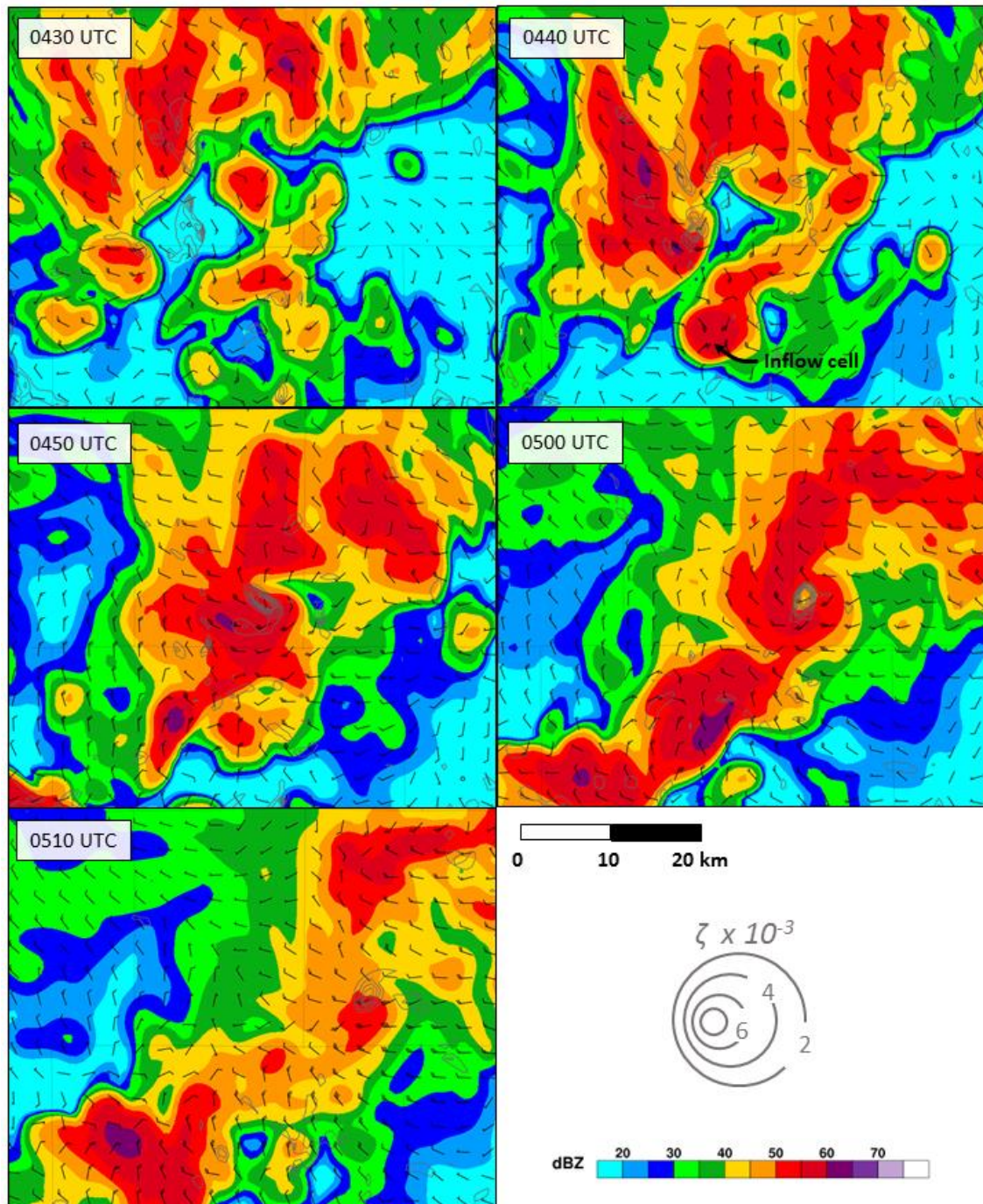


**Figure 17:** 1 km forecast surface reflectivity, vertical vorticity, and ground-relative wind barbs from 0430 - 0510 UTC in southeastern SD.



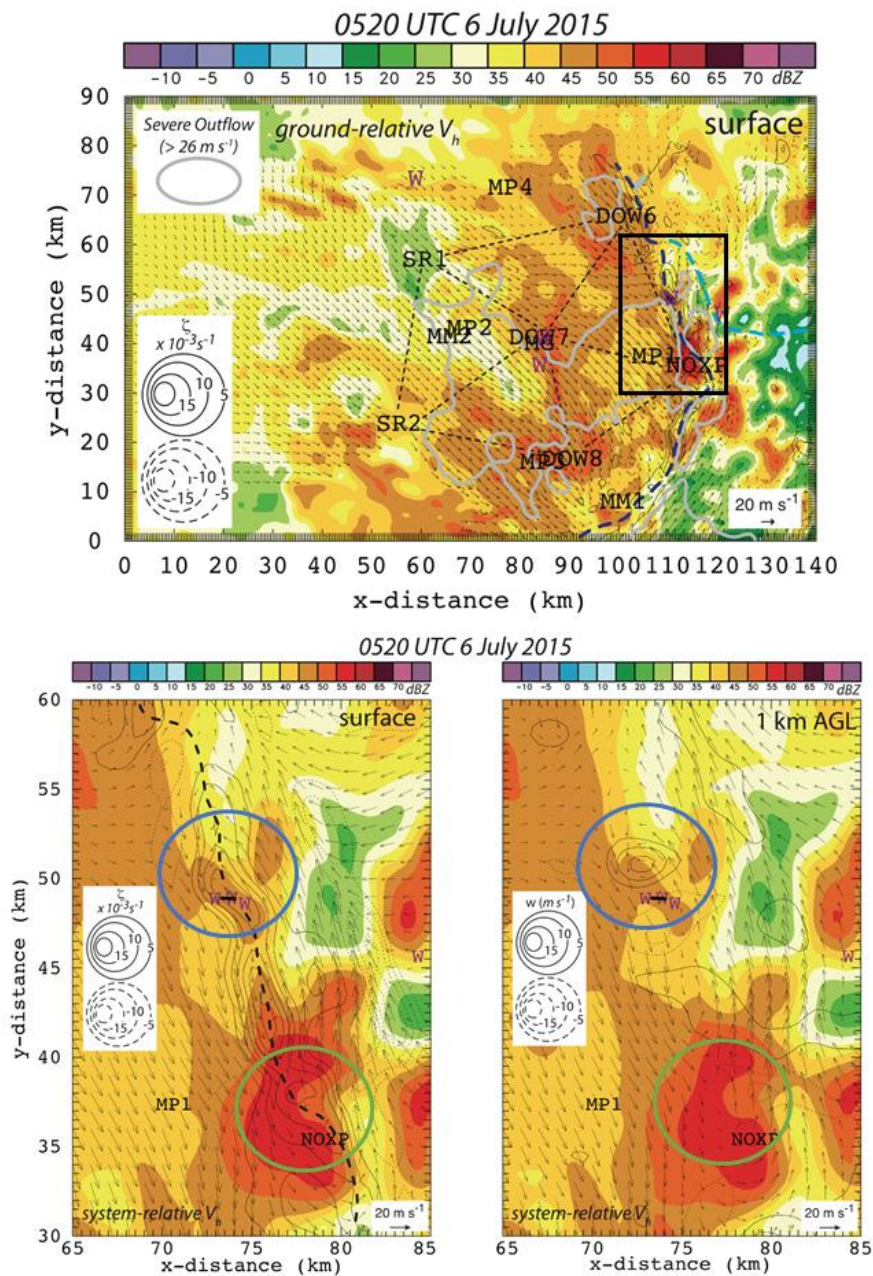


**Figure 18:** Observed analyses at 0520 UTC (courtesy of Conrad Ziegler, NSSL). Reflectivity, winds, and vertical velocity are derived using multi-Doppler analyses from multiple mobile radars. The locations and baselines of these radars are shown. Severe outflow ( $\geq 26 \text{ m s}^{-1}$ ) is highlighted with a thick, light gray line. The black box represents the domain plotted in the zoomed-in figures below. The dashed black line indicates the subjective location of the surface gust front. The strong, tornadic MV is evident (circled in blue), as well as a weakening, nontornadic MV (circled in green).

### Surface Reflectivity and Vertical Vorticity

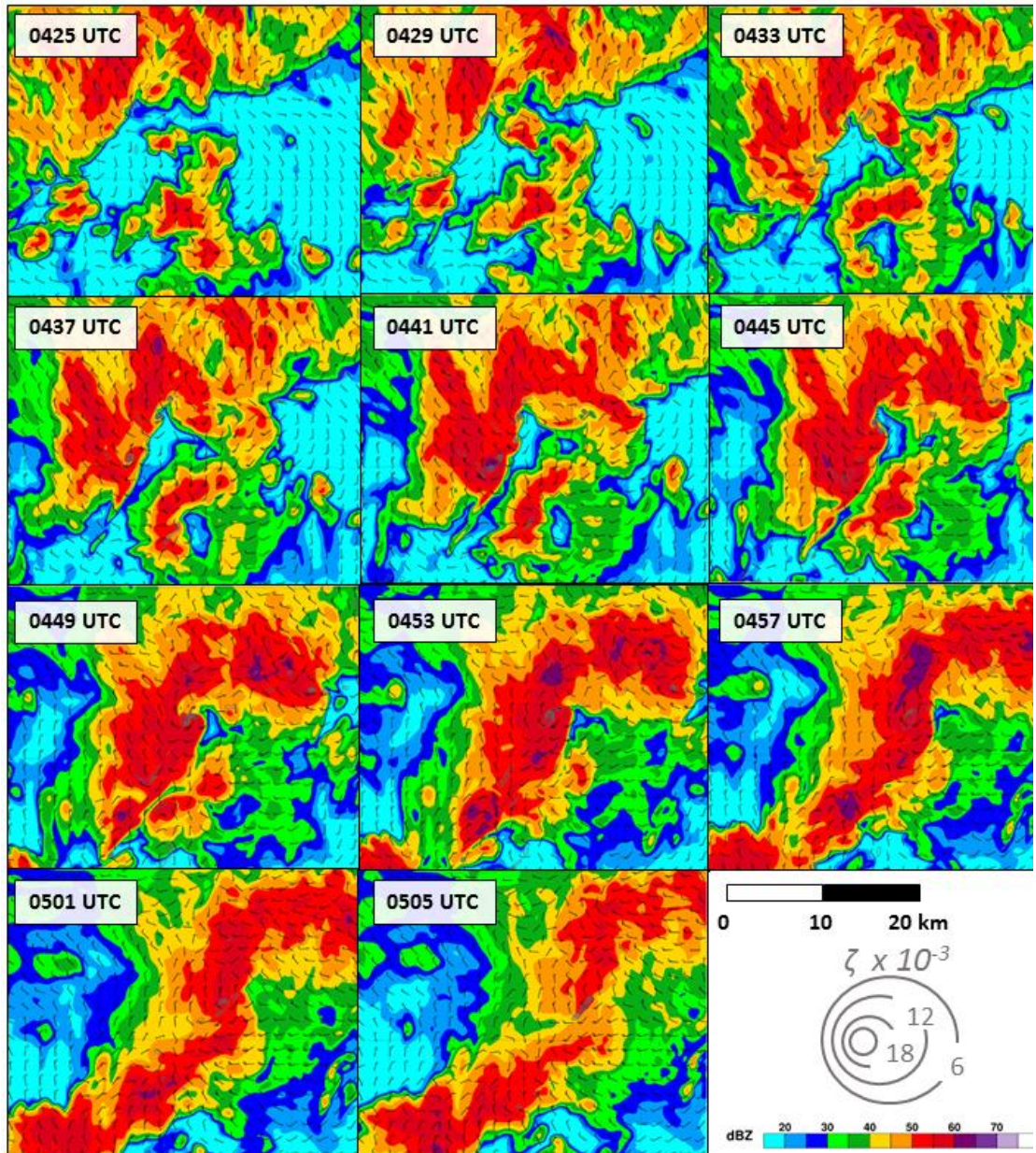


**Figure 19:** As in Fig. 17, except from 0425 - 0505 UTC on the 333 m forecast grid.

### 0-1 km SRH and 1 km AGL Vertical Vorticity

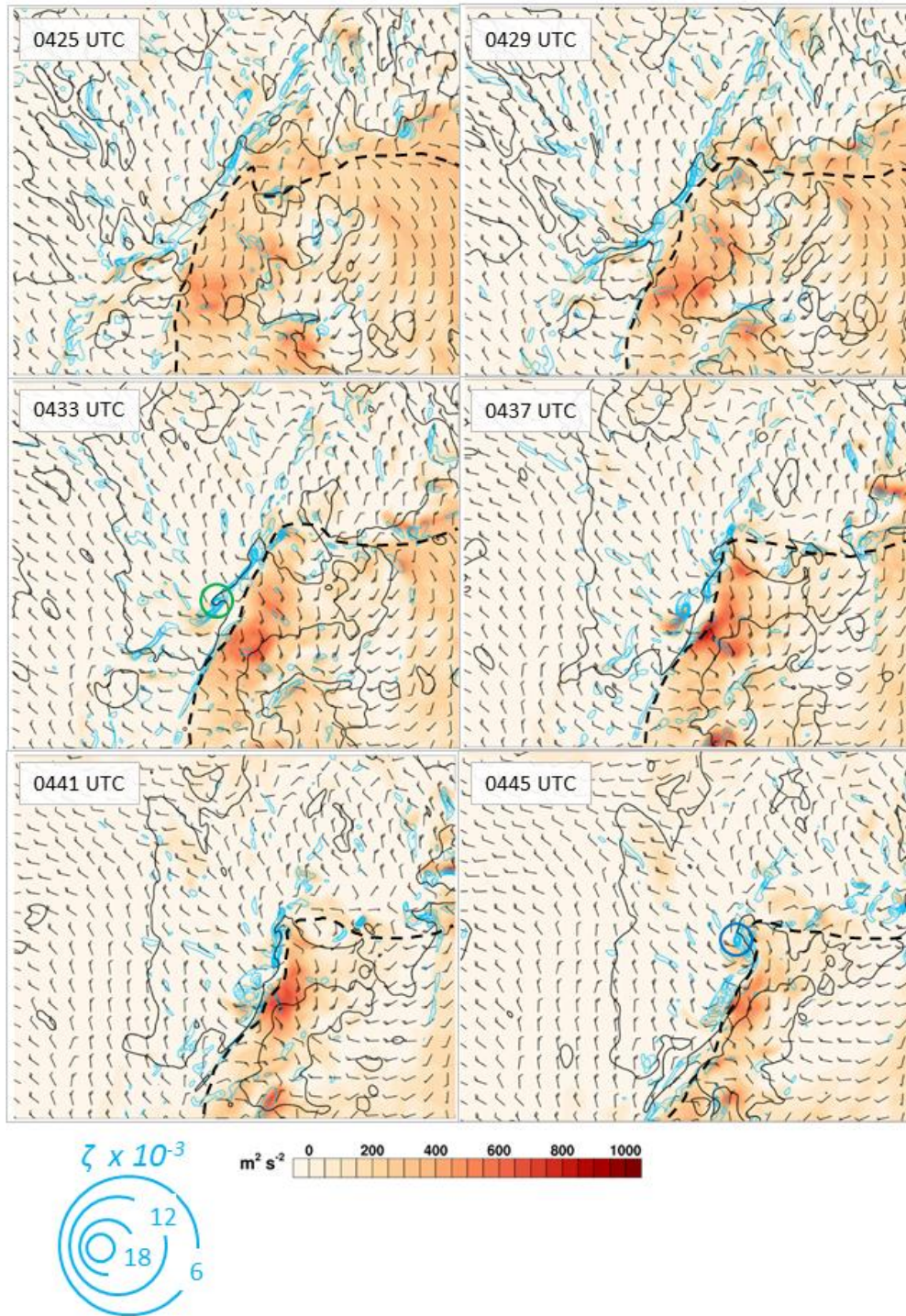


**Figure 20:** 0-1 km storm-relative helicity (SRH; shaded) and 1 km AGL vertical vorticity (contoured). Surface ground-relative wind barbs are shown, along with the subjective location of the primary gust front (dashed black line). The location of the southern (northern) MV at 0433 (0445) UTC is indicated with a green (blue) circle.

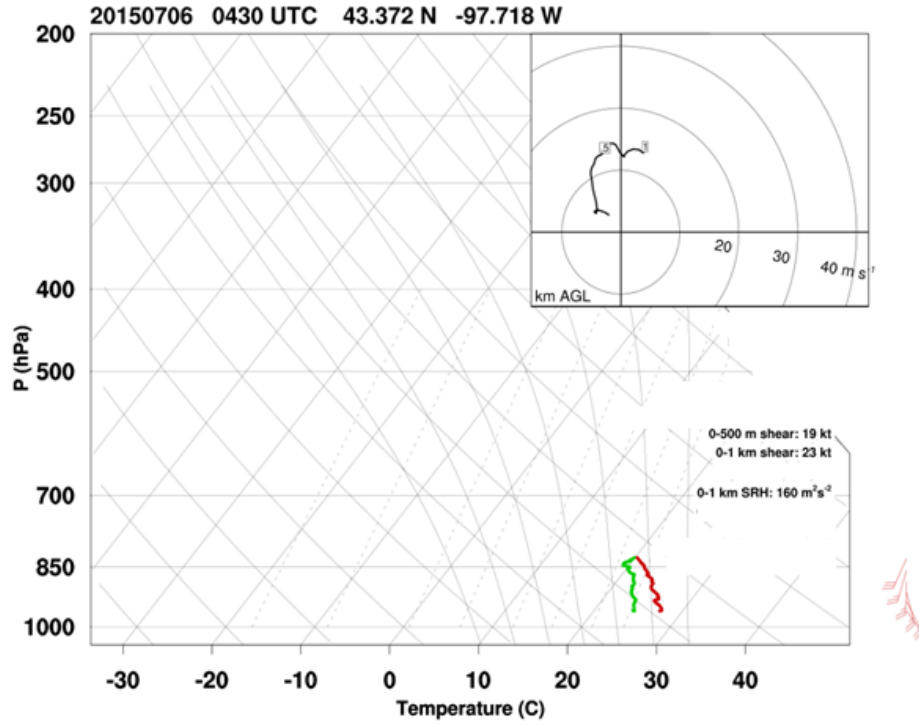


**Figure 21:** Partial observed sounding from MG1 at 0430 UTC south of an inflow cell. The sonde signal was lost near 800 mb, but collected sufficient data for low-level SRH calculations. Note that the subsequent storms had a motion closer to 15 kt at 280°, so low-level SRH was likely higher than the values shown here.

### CLAMPS Doppler Wind LIDAR Vertical Profiles

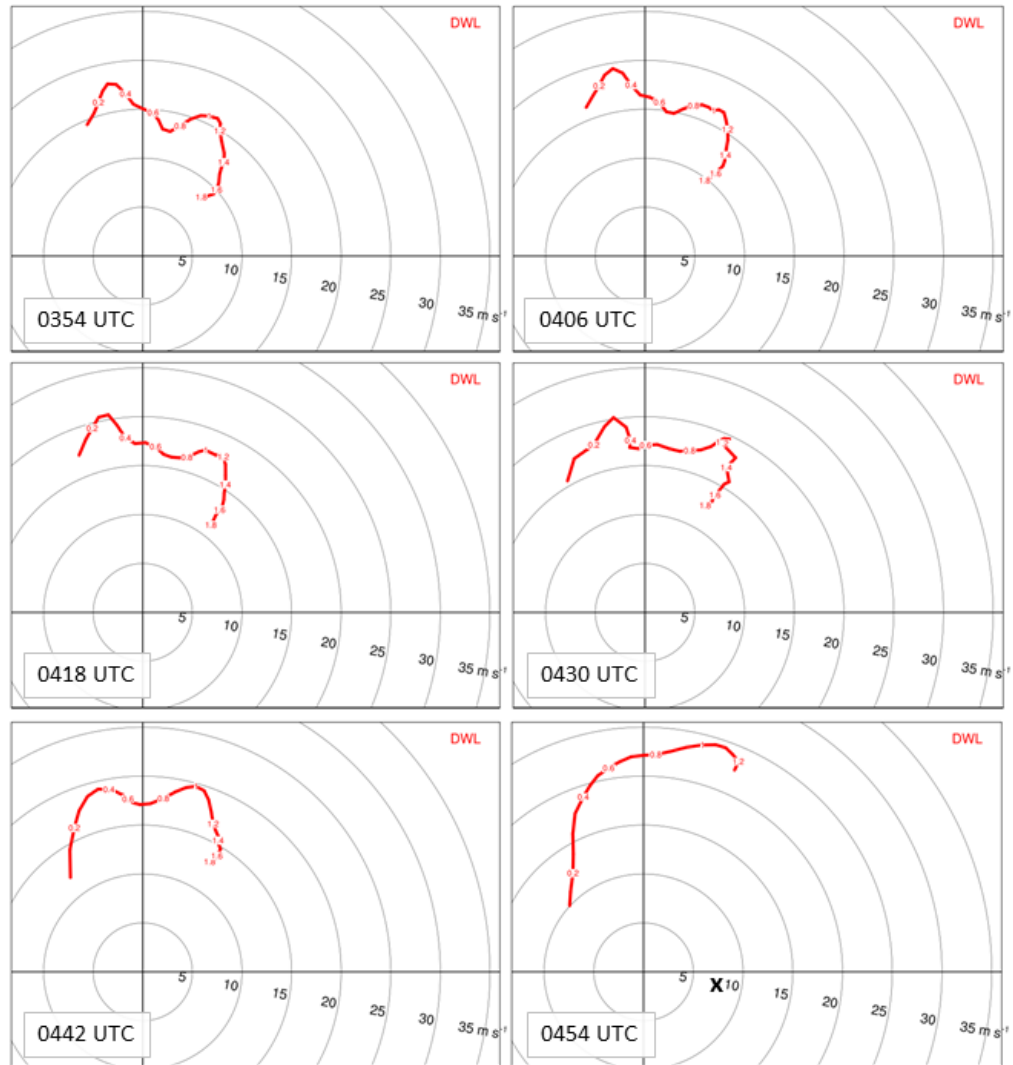


**Figure 22:** Low-level hodographs obtained from the Doppler wind LIDAR (DWL) aboard the CLAMPS platform from 0354 - 0454 UTC. Immense strengthening of winds near 1 km AGL is evident from 0354 - 0454 UTC, resulting in an environment with a significant amount of low-level SRH. The “X” in the lower right panel represents the approximate observed motion of the MVs.

## Surface $\theta_e$ -deficit and Vertical Vorticity

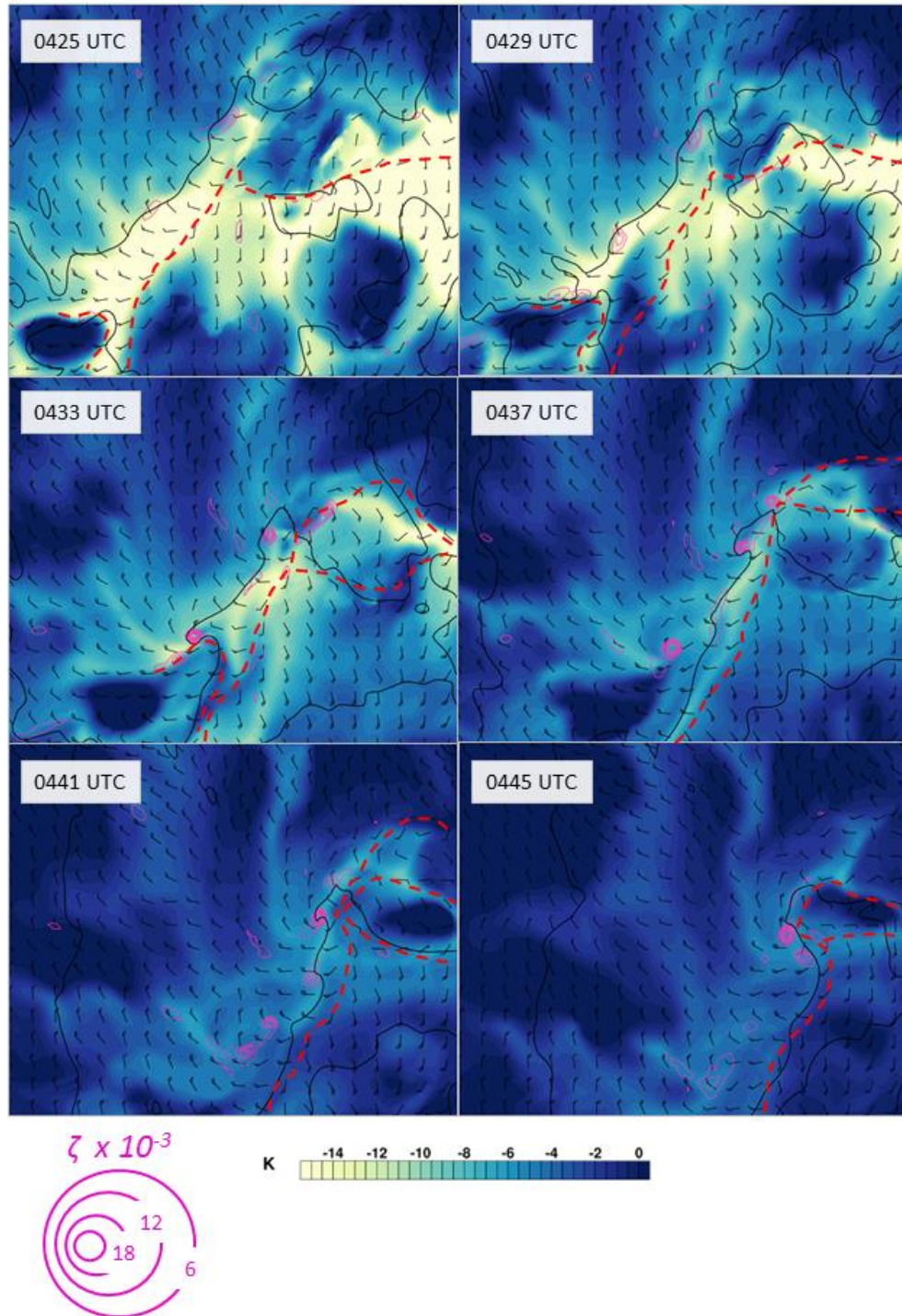


**Figure 23:** As in Fig. 20, except with surface  $\theta_e$ -deficit and surface vertical vorticity. The subjective positions of gust fronts and outflow boundaries at the surface are denoted with dashed, red lines.

### Near-surface Horizontal Vorticity and 1 km AGL Vorticity

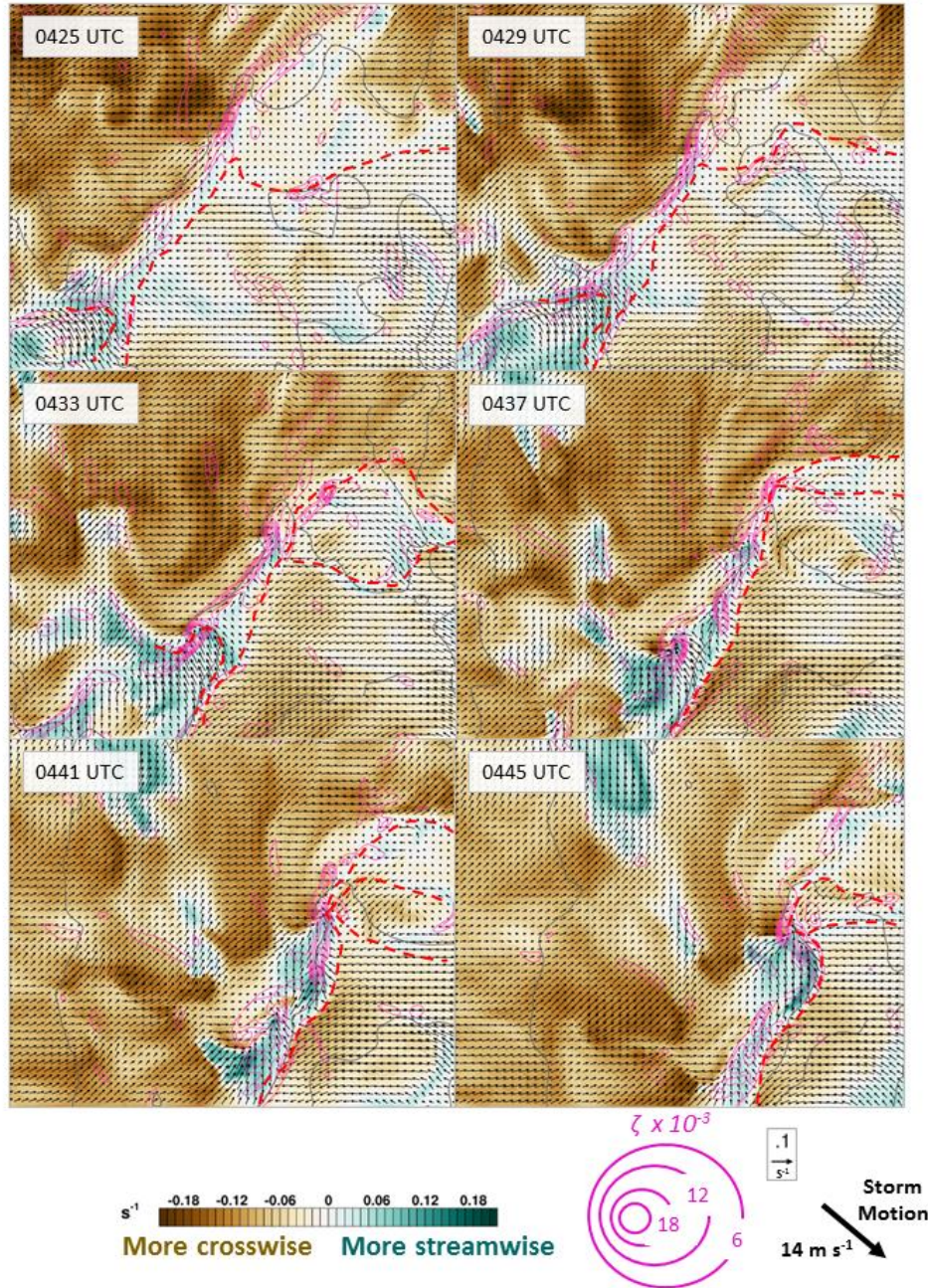


**Figure 24:** As in Fig. 23, except with vertical vorticity (contoured in pink) and horizontal vorticity near the surface (arrows). The shading represents the difference between the streamwise and crosswise components of the vorticity. Positive (green) areas represent flow that contains more streamwise than crosswise near-surface (i.e. second-lowest model level, ~30 m AGL) horizontal vorticity. The subjective locations of surface gust fronts and outflow boundaries are denoted with dashed, red lines. The storm motion used to calculate storm-relative flow is shown.

### 0-1 km AGL Horiz. Vorticity and 1 km AGL Vert. Vorticity

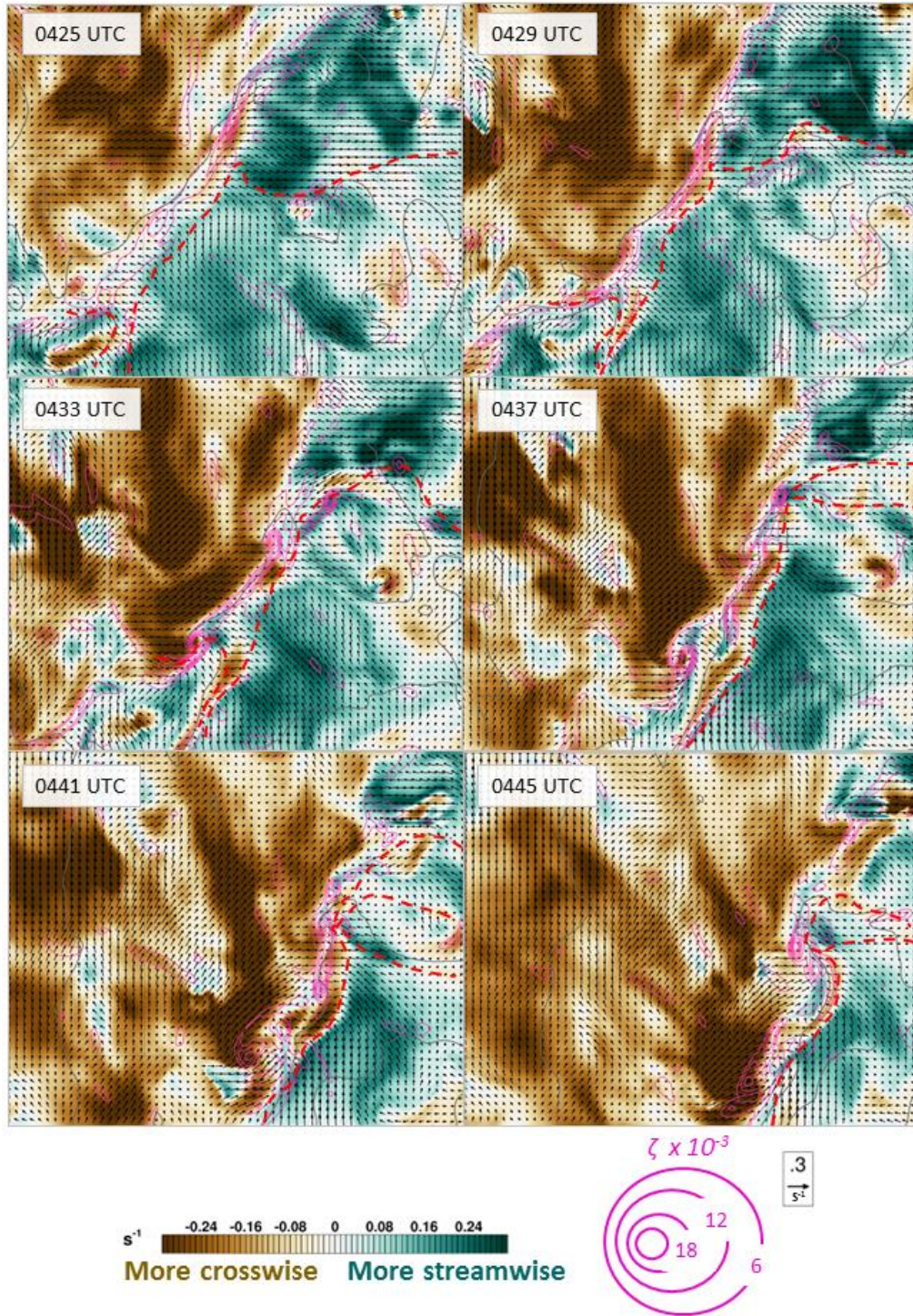


**Figure 25:** As in Fig. 24, except for 0-1 km AGL horizontal vorticity. The same storm motion was used for storm-relative flow calculations.



### 30 m AGL Horiz. Vorticity Tilting – Southern MV

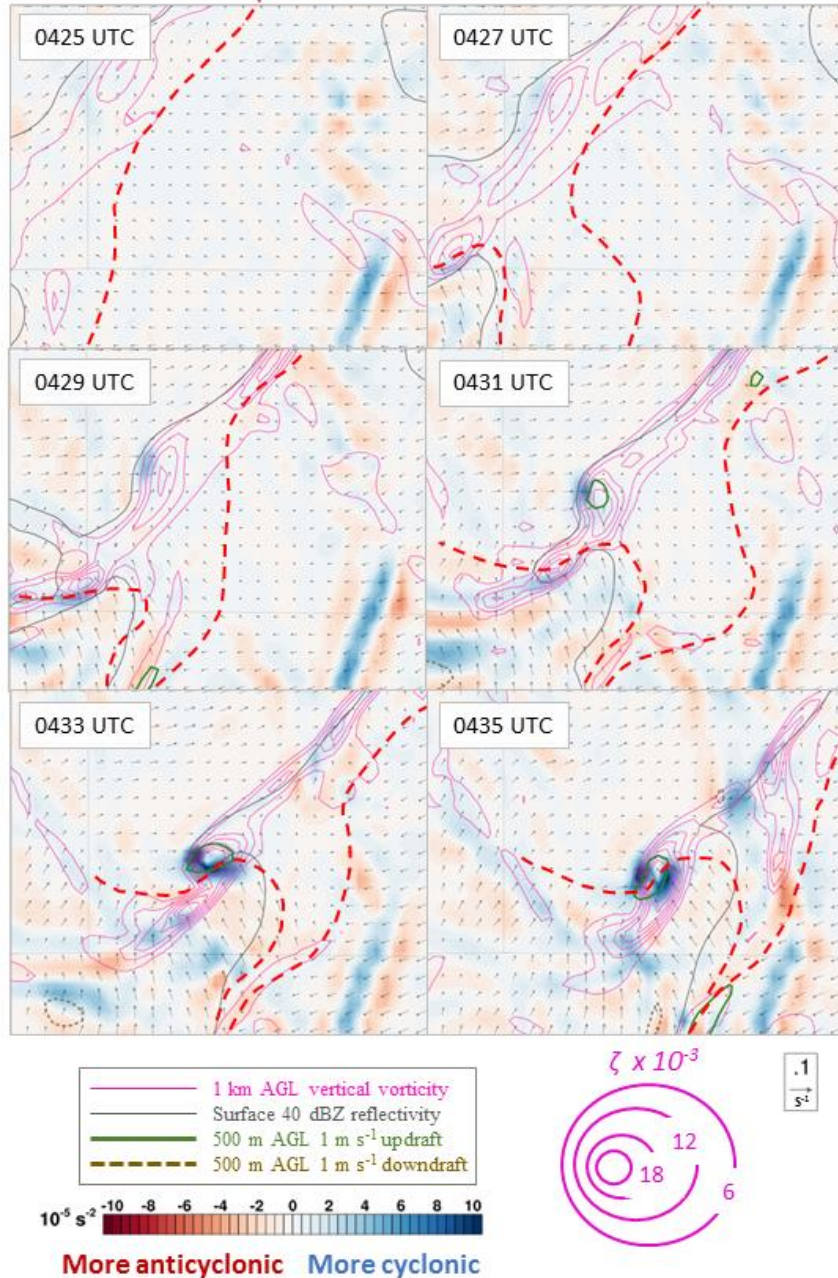


**Figure 26:** Zoomed-in view of the strengthening phase of the southern (stronger) MV. 30 m AGL horizontal vorticity tilting is shown, along with 1 km AGL vertical vorticity (contoured in pink), surface reflectivity  $\geq 40$  dBZ (gray contour), and 500 m updraft (solid green line) and downdraft (dashed brown line). Arrows represent horizontal vorticity at 30 m AGL. The subjective locations of surface gust fronts and outflow boundaries are denoted with dashed, red lines.

### 30 m AGL Horiz. Vorticity Tilting – Northern MV

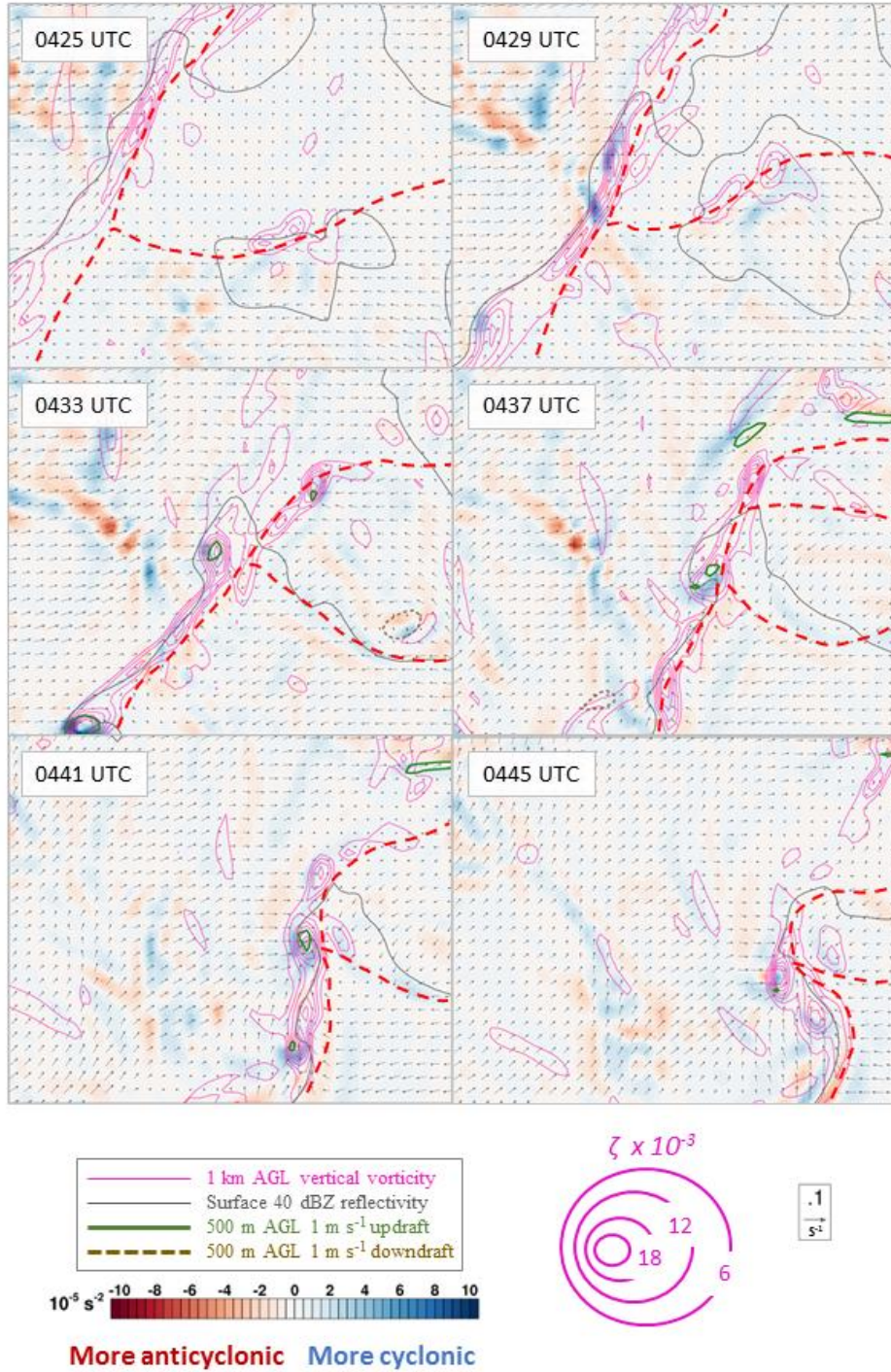


**Figure 27:** As in Fig. 26, except for the northern simulated MV from 0425 - 0445 UTC.

### 300 m AGL Vert. Vorticity Stretching – Southern MV

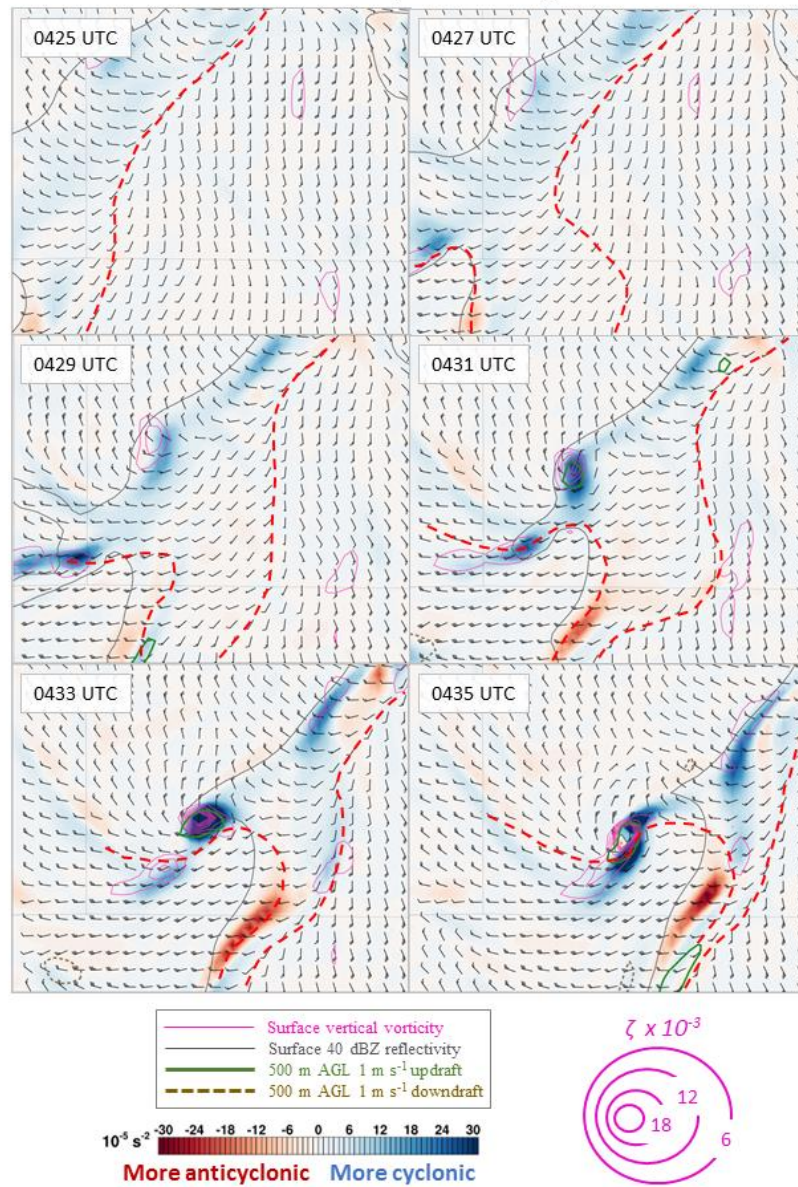


**Figure 28:** Zoomed-in view of the southern MV during its development phase. 300 m AGL stretching of vertical vorticity is shaded, along with surface vertical vorticity, surface reflectivity, and 500 m AGL updraft and downdraft. Surface ground-relative wind barbs are shown. Subjective locations of surface gust fronts and outflow boundaries are denoted with dashed, red lines.

### 300 m AGL Vert. Vorticity Stretching – Northern MV

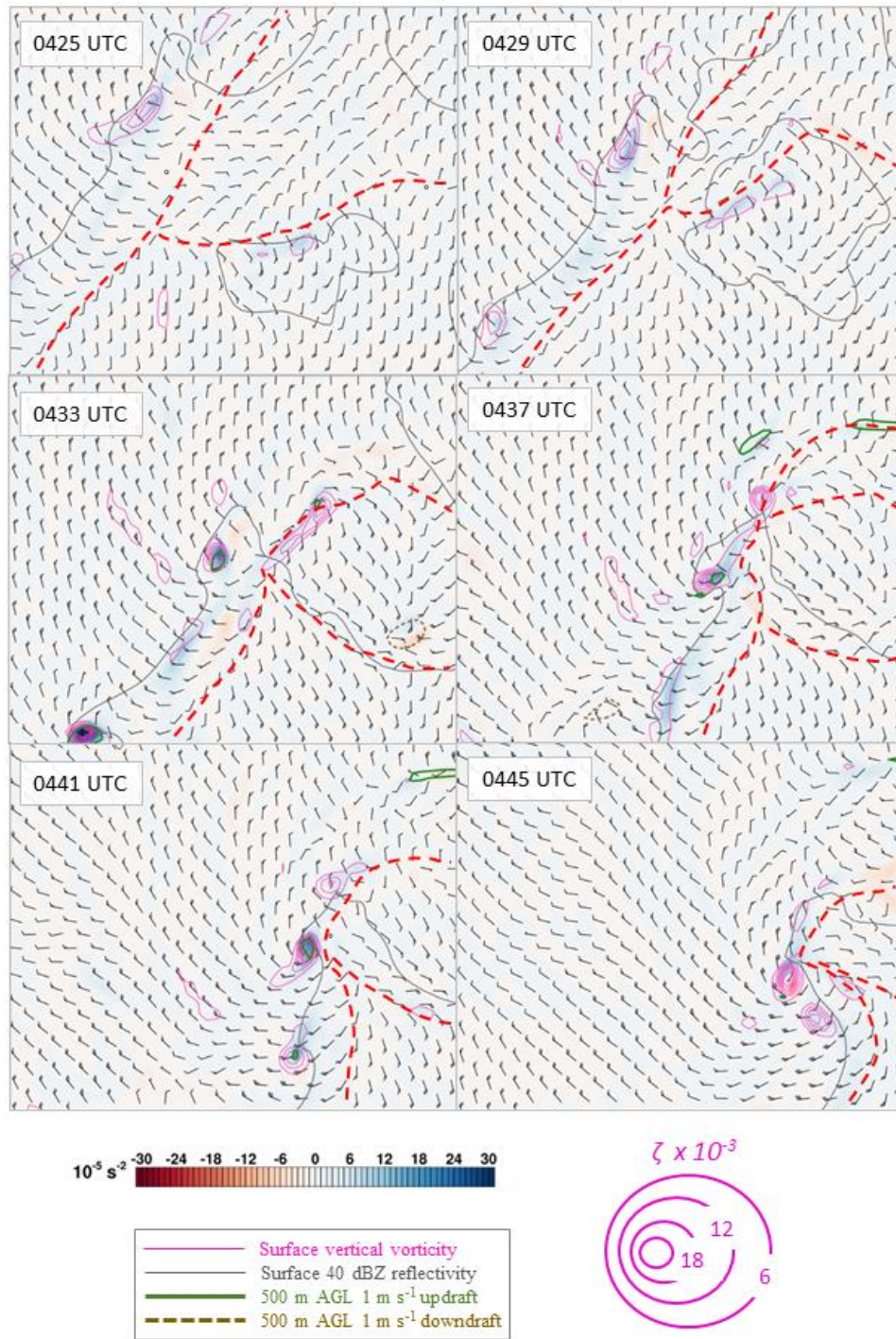


**Figure 29:** As in Fig. 28, except for the northern simulated MV from 0425 - 0445 UTC.

## Lagrangian Trajectories and Vorticity Budgets

Member 30 (0423 - 0433 UTC)

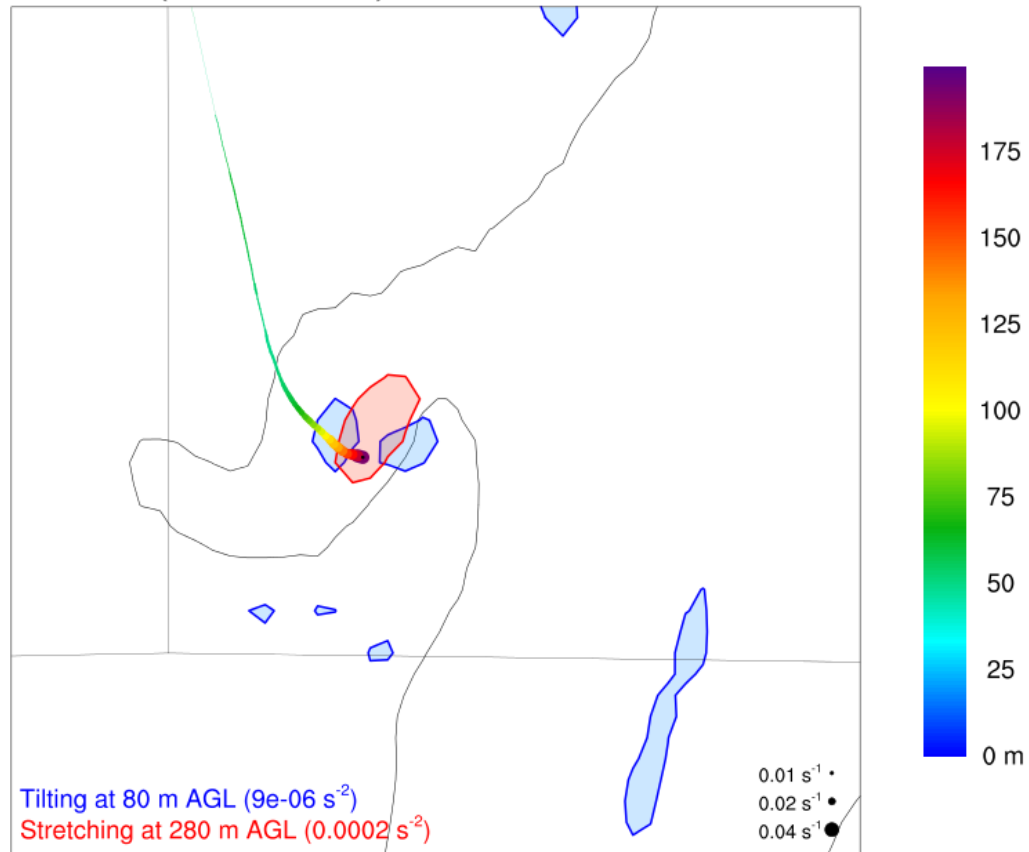


**Figure 30:** Horizontal trace of a parcel entering the low-level MV. Heights AGL are colored along the 10-minute backward trajectory according to the color bar, and the width of the trace is proportional to the magnitude of the parcel's vertical vorticity (see the bottom right corner of the plot). Stretching  $\geq 0.0002 \text{ s}^{-2}$  at 280 m AGL and tilting  $\geq 0.000009 \text{ s}^{-2}$  at 80 m AGL at 0433 UTC are shaded in red and blue, respectively. The 40 dBZ reflectivity contour at 0433 UTC is shown as a light gray line.

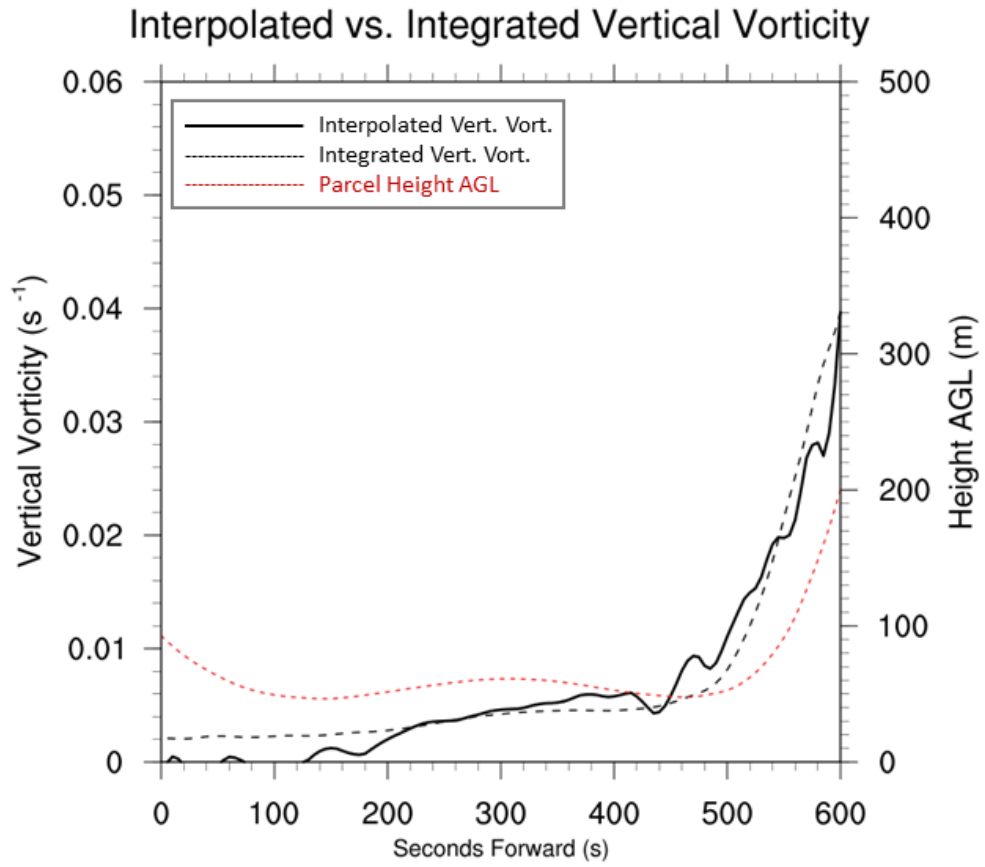


**Figure 31:** Time-series of interpolated and integrated vertical vorticity and parcel height along a Lagrangian trajectory entering the low-level MV.

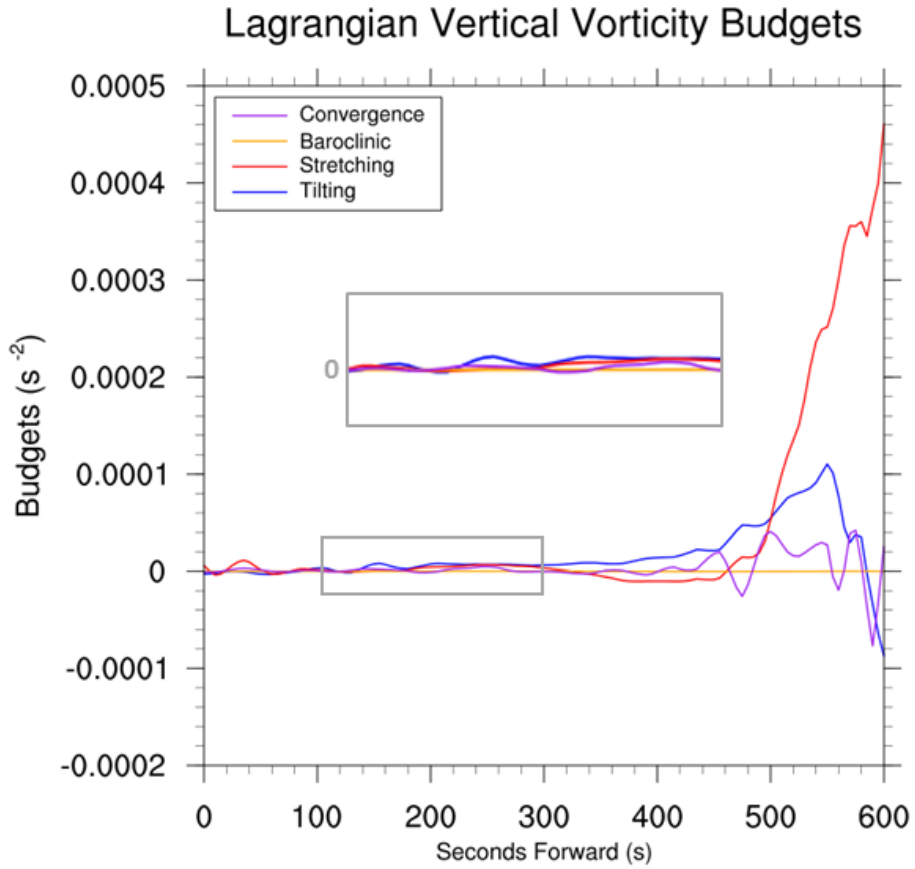


**Figure 32:** Time-series of vertical vorticity budget terms for the same parcel shown in Fig. 30. The inset shows a zoomed-in view of the 100-300 s timeframe, in which the parcel first consistently acquires positive vertical vorticity near 50 m AGL.